Department of Physics and Astronomy

University of Heidelberg

Master thesis in Physics

submitted by

Hyoyin Gan

born in Ulsan, Republic of Korea

February 2017

Nuclear reactions in astrophysical plasmas

This Master thesis has been carried out

by Hyoyin Gan

at the Max-Planck-Institut für Kernphysik

under the supervision of

Priv.-Doz. Dr. Adriana Pálffy

Kernreaktionen in Astrophysikalischen Plasmen

Der langsame Neutroneneinfangprozess während der Nukleosynthese bewirkt oftmals, dass Kerne, die einem Neutroneneinfang oder Beta-Zerfall unterliegen, nicht nur in ihren Grundzuständen, sondern auch in langlebigen angeregten Zuständen, in sogenannten Isomeren, vorzufinden sind. Solche Isomere können außerhalb des thermischen Gleichgewichtes mit den Grundzuständen der Kerne sein, und müssen deshalb gesondert berücksichtigt werden. In dieser Arbeit untersuchen wir theoretisch die Abregung solcher Isomere infolge von Kernanregung durch Elektroneneinfang (NEEC) unter den Bedingungen des langsamen Neutroneneinfanges in dichten, stellaren Plasmen. Aufgrund der hohen Ladungszustände in diesen Plasmen ist NEEC nicht notwendigerweise ausbalanciert mit ihrem inversen Prozess, der inneren Konversion, weshalb die Reaktionsraten getrennt betrachtet werden können. Wir analysieren die Fälle ^{58m}Co, ^{99m}Tc, ^{121m}Sn, ^{121m}Sb und ^{152m}Eu, und vergleichen die NEEC Abregungsraten mit den relevanten Beta- und Gamma-Zerfallsraten der Isomere. Die Ergebnisse für ^{58m}Co, ^{121m}Sb und ^{152m}Eu zeigen, dass NEEC als wichtiger Abregungskanal der Isomere in astrophysikalischen Plasmen betrachtet werden sollte.

Nuclear Reactions in Astrophysical Plasmas

In the process of slow neutron capture nucleosynthesis, one often has to take into account that nuclei undergoing neutron capture and beta decay may not be only in their ground states, but also in long-lived excited states, known as nuclear isomers. Such isomers might not be thermally equilibrated with the nuclear ground states. In this thesis, we theoretically investigate the efficiency of nuclear excitation by electron capture (NEEC) to deplete such isomeric states in dense stellar plasmas under the s-process conditions. Due to the high charge states available in such plasmas, NEEC is not always accompanied by its detailed-balance counterpart, the inverse process internal conversion, and reaction rates can be considered separately. We investigate the cases of ^{58m}Co, ^{99m}Tc, ^{121m}Sn, ^{121m}Sb and ^{152m}Eu and compare the NEEC depletion rates with relevant beta and gamma decay rates of the isomeric states. The results for ^{58m}Co, ^{121m}Sb and ^{152m}Eu show that NEEC should be considered as relevant isomer depletion channel in astrophysical plasmas.

Contents

Chapter 1

Introduction

The origin of matter has been one of the most fundamental questions throughout human history. The universe was started from one tremendous explosive event 13.7 billion years ago—the Big Bang. The universe was originated from a very small point which had unimaginably high density of energy. Approximately 10^{-43} second after the Big Bang, the universe was a region of only 10^{-35} m and had a temperature of over 10^{32} K. As the universe cooled and expanded, conditions became suitable to give rise to the building blocks of matter—the quarks and electrons which all matter is made of. Particles and antiparticles were being created from energy and they were also being combined together to annihilate and release energy. About 10^{-5} second after the Big Bang at temperature of about 10^{13} K, quarks aggregated and started to produce protons and neutrons. The lower temperature allows quark and anti-quark pairs to combine into mesons. At this moment, the formation of atom was not yet possible, because the produced particles were still too energetic to be stabilised. The neutrons were being created and destroyed by the reaction between protons and electrons. The protons and electrons were being combined to form neutrons and neutrons were decaying into protons and electrons:

$$\begin{aligned} p^+ + e^- &\rightleftharpoons n + \nu_e, \\ n &\rightleftharpoons p^+ + e^- + \overline{\nu}_e. \end{aligned} \tag{1.1}$$

From around 1 second to 3 minutes after the Big Bang, the temperature is estimated to have decreased from 10^{10} to 10^9 K. At this temperature, neutrons and protons collisions were finally resulting in the formation of nuclei. The first atomic nuclei formed. The proton itself was the nucleus of hydrogen (H). The neutron and the proton combined to form nucleus of deuterium (D). The formed Deuterium nuclei collided to produce nuclei of tritium (T) and helium (He):

$$\begin{aligned} &p^+ + n \rightarrow \mathrm{D} + \gamma, \\ &\mathrm{D} + p^+ \rightarrow {}^3\mathrm{He} + \gamma, \\ &\mathrm{D} + \mathrm{D} \rightarrow \mathrm{T} + p^+, \\ &\mathrm{T} + \mathrm{D} \rightarrow {}^4\mathrm{He} + n. \end{aligned} \tag{1.2}$$

On very rare occasions, the collisions of D and He produced lithium (Li) and beryllium (Be), respectively. This Big Bang nucleosynthesis is responsible for production of the

lightest primordial elements from ^{1}H to ^{7}Li. The produced elements precede star formation and stellar nucleosynthesis. No nucleosynthesis can proceed beyond Li until stars form.

The universe continued to expand and cool, the atoms of gases collected to form clouds of H gas. There were no stars or planets yet. About 10^8 years after the Big Bang, these massive gas clouds were contracting due to their own gravity and this gravity increased pressure and temperature. At the center of these gases, the pressure and temperature were so high that atoms did not exist. Rather, the electrons were stripped from the atoms and the electrons and nuclei were moving randomly with very high speed in the core. Once the temperature reached $\sim 10^7$ K, the H nuclei in the core were energetic enough to collide and fuse to form He nuclei and release a huge amount of energy. The released energy from the core counteracted the gravity. If the outward pressure of fusion energy was balanced by the inward pull of gravity, the gas clouds reached equilibrium and the star formed.

Stars are powered by nuclear fusion, in which light nuclei combine to make heavier nuclei. For most of a star's life, the main fusion process is H burning to form He [1]. Once the H in the core of a star is used up, and if the star is massive enough, it contracts, heats up and starts to fuse He to carbon (C). Similarly, after the main source of He in the core is exhausted, one can combine elements to get heavier nuclei. However, the amount of energy per mass released by fusion reaction drops drastically after H→He reaction. After one gets up to iron (Fe) and nickel (Ni), further fusion require an energy input than generating output. Indeed, the stellar nucleosynthesis cannot produce nuclei beyond Fe and Ni.

Further element production proceeds via slow, rapid neutron capture (s- and r-process) and proton capture (p-process). The s- and r- processes take place through neutron captures and subsequent beta-decays. They were first identified in 1957 in a pioneering work by E. Burbidge, G. Burbidge, Fowler, and Hoyle (shortly, B^{2}FH) [2]. About half of the abundances beyond Fe in the solar system are formed by the s-process, the other half by the r-process. A small contribution is given by the p-process. Isotopes involved in s-process are often sufficiently stable and long-lived to be studied in the laboratory. For this reason, physical properties of s-process are relatively well-known thanks to astronomical observations of stars and measurement of their element abundances [3].

From the revealed physical sites of the s-process, it turns out that in the stellar environment, considering nuclei only in their ground states is not sufficient. Due to the hot plasma temperature, excited nuclear states can be significantly populated [4–7], typically according to a Maxwell-Boltzmann distribution. However, a special role is played by nuclear isomers, i.e., long-lived excited nuclear states [8, 9]. These can be directly populated by gamma decay cascades following neutron capture [10, 11] and can have beta decay rates very different from the ones of the nuclear ground states [12, 13]. Due to their long lifetime, equilibration with the ground state and the other non-isomeric excited states is not always possible [14]. In this case, one needs to include the isomers as additional nuclear species in the nucleosynthesis nuclear reaction networks under stellar conditions.

A so-far not so well investigated coupling between the ground and isomeric nuclear

states can occur via nuclear excitation by electron capture (NEEC). In this process, a free electron is recombined into the bound state of a highly-charged ion with the simultaneous excitation of the nucleus [15–20]. NEEC is the time-reversed process of internal conversion (IC), in which the nucleus de-excites by kicking out a bound electron. Although one would therefore expect that the NEEC and IC rates are always connected in the astrophysical plasma via the principle of detailed balance, IC might be hindered by channel closure due to fast collisional and photo-ionisation in the plasma.

In this work, we investigate the efficiency of depleting the isomeric state via NEEC in the dense astrophysical plasmas. We consider here a selection of isomers: ^{58m}Co, ^{99m}Tc, ^{121m}Sn, ^{121m}Sb and ^{152m}Eu. For the NEEC calculations in the plasma environment, we take into account: (i) details about conditions and fluxes, plasma compositions as for s-process; (ii) the specific charge states under these conditions, and calculate total depletion rates for a number of possible recombination channels.

Our calculations are founded on the theoretical treatment of NEEC developed in Ref. [16]. With the local thermodynamic equilibrium (LTE) assumption, the degree of ionisation of ions is computed by solving the Saha equation [21]. Combining the NEEC transition rates, degree of ionisation and the electron flux from the Fermi-Dirac integral, the NEEC reaction rate in the plasma is obtained. The obtained reaction rates are compared with beta decay rates of the isomeric states. As a result, we find high reaction rates for ^{58m}Co, ^{121m}Sb, and ^{152m}Eu; and rather low rates for ^{99m}Tc and ^{121m}Sn. Based on the promising examples of ^{58m}Co, ^{121m}Sb, and ^{152m}Eu, we conclude that NEEC should be considered as relevant isomer depletion channel in astrophysical plasmas.

This thesis is structured as follows: In Chapter 2, we introduce the ceoncept of neutron capture nucleosynthesis. Various processes involved in nucleosynthesis scenarios are discussed first and the physical sites and conditions of neutron capture processes are identified. In Chapter 3, local thermodynamic equilibrium (LTE) is discussed. Based on the LTE assumption, the Saha ionisation is introduced to describe the charge state of ions in the plasma. To examine the equilibration of nuclear states, two-level and three-level system formalisms are discussed. Chapter 4 is devoted to the theoretical treatment of nuclear excitation by electron capture. Numerical results are presented and discussed in Chapter 5. Finally, the work concludes with a summary and outlook.

Chapter 2

Neutron Capture Nucleosynthesis

2.1 Nucleosynthesis

In the first three minutes after the Big Bang, most of the hydrogen (H) and helium (He) and a small amount of lithium (Li) were produced. Two more light elements, beryllium (Be) and boron (B) were synthesised in interstellar space by collisions between cosmic rays and gas nuclei [1]. The process that happened in the first three minutes after the Big Bang is called *Big Bang Nucleosynthesis* (BBN).

While H and He are the oldest elements in our Universe, and more than ninety percent of the Universe is made up of them, simply having H and He does not allow for nature to create complex organic matter and life. To do this, heavier elements are needed, for instance, carbon (C), oxygen (O) and nitrogen (N) [22]. Heavier elements from carbon to iron are produced by charged-particle fusion reactions in stars during stellar evolution. This process is called *stellar nucleosynthesis*. H, He and the traces of Li, Be, and B produced in the BBN have served as the source elements for the formation of stars long after the BBN stopped. Fusion reactions in stars are then responsible for the formation of heavier elements. Fusion reactions are exothermic processes and the released energies are used to power stars and overcome gravitational contraction. Most of a star's life is devoted to the fusion process where H is burned to form He.

The binding energy per nucleon increases with nuclear mass up to ^{56}Fe, the most tightly bound of all nuclei. The production of any heavier elements by direct fusion is endothermic. Moreover, as the proton number increases, the Coulomb barrier increases. For sufficiently high proton numbers, the Coulomb barrier between protons is too strong that two positively charged nuclei cannot overcome it and reach separation distances where strong force dominates. Therefore, the isotopes of elements beyond Fe are produced mostly by neutron-capture processes (n-capture) but not by nuclear fusions. These processes are recognised as *neutron capture nucleosynthesis* and their products are referred to as n-capture elements [1].

The n-capture process iterates a two-step sequence : (i) a seed nucleus captures free neutrons until it forms an unstable isotope; (ii) the unstable isotope increases the number of nuclear protons (Z) by one (Z+1) via beta decay and creates a new element. The resulting nucleus is heavier than the seed nucleus and has less binding energy per nucleon, but the additional binding of the free neutrons makes the process exothermic [23]. Sources of free neutrons are available from interior fusion layers during late quiescent evolutionary stages of stars over a wide mass range [24].

Mainly, there are two different types of n-capture processes for astrophysical nucle-

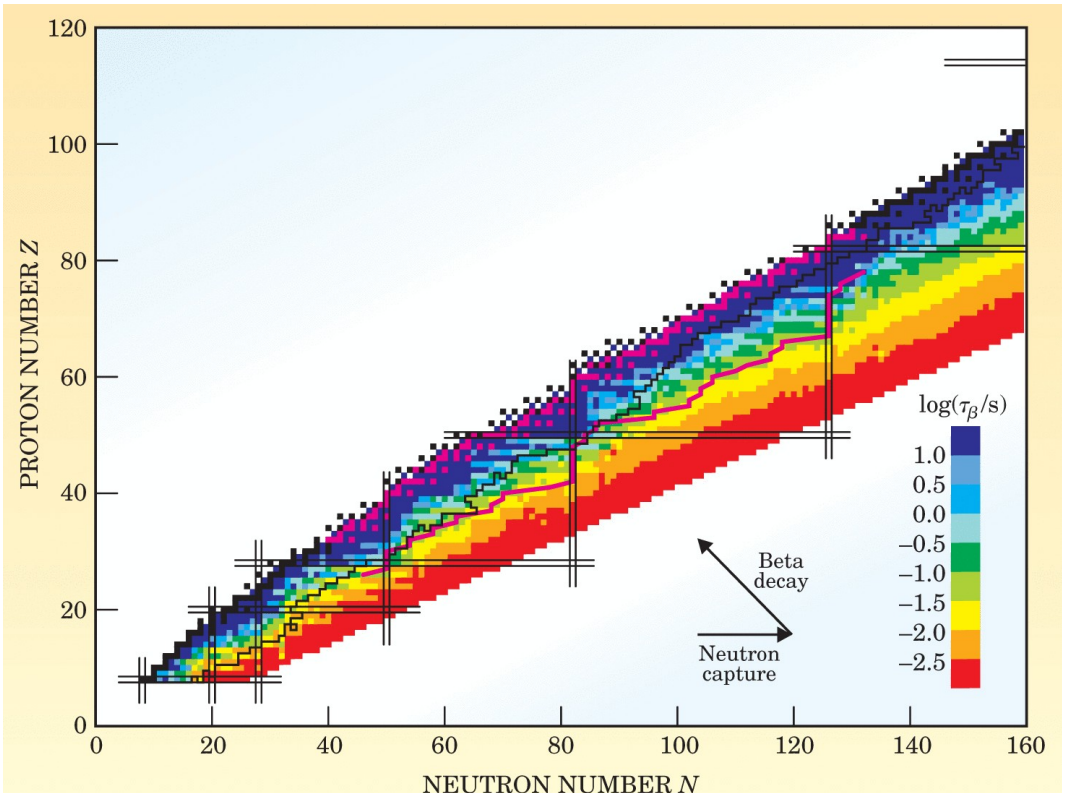

Figure 2.1: Chart of nuclides. The diagram plots the number of protons (Z) against the number of neutrons (N) for the stable and neutron-rich unstable nuclides. Stable isotopes against beta decay are indicated by black and magenta dots, and they form *the valley of stability* that runs along the top edge of the band. The jagged black line is the limit of laboratory information. The jagged magenta line shows a typical path of rapid neutron captures (r-process). Such paths tend to turn vertical at the double vertical lines that mark neutron numbers corresponding to closed neutron shells. The horizontal double lines indicate closed proton shells. Coloured bands describe the measured or predicted beta decay lifetimes τ_β (taken from Ref. [1]).

osynthesis [2]. These two processes are called the slow (s) and rapid (r) neutron capture processes. A process is determined to be *slow* or *rapid* by comparing the time scale of n-capture and beta decay. After a nucleus has captured a neutron, the time scale τ_n for it to capture an extra neutron can be competing with the time scale τ_β for it to undergo beta decay. While τ_β is equivalent to the beta decay life time, τ_n highly depends on the neutron flux of the environment.

In the s-process, τ_n is much longer than τ_β, i.e., $\tau_\mathrm{n} \gg \tau_\beta$. Indeed, a single n-capture is generally followed by beta decay. On the other hand, the path charted by successive n-captures is close to the *valley of β-stability* as shown in Fig. 2.1. From the figure, one

can clearly see that for a given proton number, the beta decay lifetime is decreasing as the neutron number is increasing.

In the r-process, τ_β is required to be much longer than τ_n, i.e., $\tau_\beta \gg \tau_\mathrm{n}$. This condition is achieved in extremely neutron-rich environments, as τ_n is inversely proportional to the neutron density of the environment [25]. Such high neutron fluxes are available, for example, in a supernova explosion. In this case, the nuclei capture neutrons to become very neutron-rich and unstable isotopes which are far from the β-stable valley. Once the neutron flux is exhausted, the unstable nuclei will undergo a sequence of beta-decays until the first stable nucleus is formed.

However, for some mass numbers, two (or even three) stable nuclei exist. The parent nucleus which undergoes the r-process will stop in the nucleus which has the larger neutron number; therefore, for a given mass number, the nucleus with a smaller neutron number will not be created by the r-process, rather it will be produced from the s-process. Such nuclei are called *s-process only* nuclei. In the same manner, the neutron-rich nuclei produced from r-process are called *r-process only* nuclei and their abundances are purely produced by the r-process. S-process only and r-process only nuclei play an important role, as they have a unique contribution in the nucleogenesis process [25]. While the specific physical conditions and nuclear properties of the s-process are well-known, physical properties of r-process, especially its astrophysical sites, have not yet been clearly identified [1]. In addition, a detailed analysis of Fig. 2.1 suggested that the most proton-rich nuclei cannot be produced by n-capture processes. The stable isotopes of proton-rich nuclei between ^{74}Se and ^{196}Hg have 10 to 100 times less abundances than the abundances of s- and r-process nuclei. These nuclei are assumed to be produced from the *p-process*, either by proton captures (p,γ) or photodisintegration reactions [26]. Unfortunately, p-process produced nuclides (p-nuclei) are not well identified and their origin is still not completely understood. In Subsec. 2.1.1 and 2.1.2, some properties of the s- and r- processes will be discussed in detail, following [1, 23] and the Chapter 5 of Ref. [25].

2.1.1 The s-process

The essential features of the *slow* neutron capture process were already investigated by B^{2}FH [2, 27]. The He-burning layers of low-mass asymptotic giant branch (AGB) stars (produce main s components) and the He- and C-burning phases of massive stars (produce weak s components) are the astrophysical sites of the s-process [28]. In the s-process, heavy nuclei are formed by a sequence of n-captures and beta decays, mostly processing the elements below and near the iron peak into a wide range of nuclei extending up to Pb and Bi [25]. With the s-process fulfilling the condition that $\tau_\beta \ll \tau_\mathrm{n}$, the s-process path runs along the valley of beta-stability in the nuclear chart. Therefore, isotopes involved in s-process nucleosynthesis are sufficiently long lived to be studied in the laboratory. This makes the s-process the best understood process among different processes in the nucleosynthesis. The involved n-capture cross sections and half-lives can be determined in the laboratory. The remained uncertainties in s-process predictions are related to the favoured stellar sites [29].

Using the s-process abundances at the branching points and the required nuclear input (such as nuclear masses, nuclear half-lives and neutron cross sections), we can obtain the neutron density and temperature of the stellar environment where the s-process takes place. The branching points occur on the s-process path if τ_β and $\tau_{\rm n}$ are comparable. This means that the s-process path can proceed both way, by n-capture and by beta decay. The relative matter flow at the branching point depends on the ratio of n-capture and β- half-lives. As the n-capture half-life depends on the neutron density, the branching enables us to determine the neutron density once we know the β-half-lives and n-capture cross sections. For instance, in the A =147-149 mass region shown in Fig. 2.2, the branching

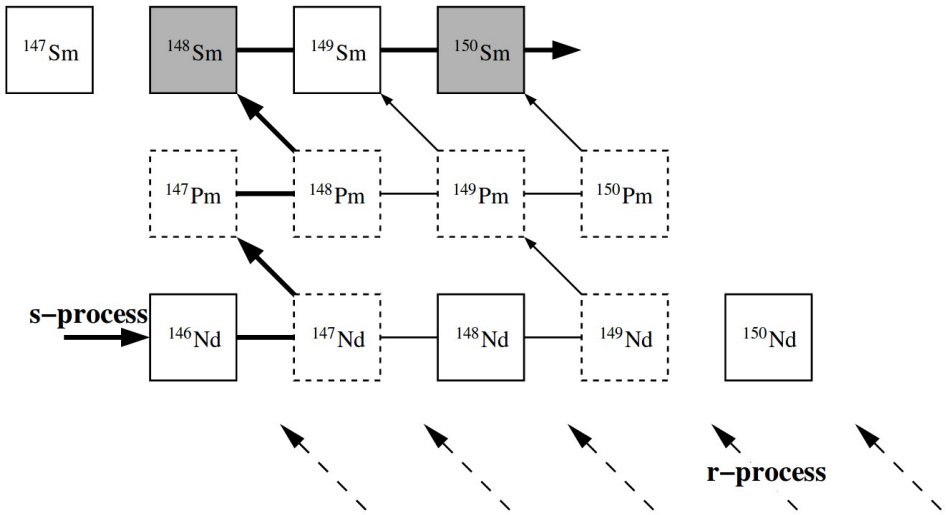

Figure 2.2: S-process reaction path in the Nd-Pm-Sm region with the branchings at A = 147, 148, and 149. Particularly, ^{148}Sm and ^{150}Sm are shielded against the r-process beta decays. Theses two isotopes define the branching (taken from Ref. [25, 26]).

points can determine the neutron density during the s-process. Here, ^{148}Sm and ^{150}Sm (Z=62) are s-process-only isotopes which are shielded against r-process contributions by the two stable isotopes ^{148}Nd and ^{150}Nd (Z=60). The relative abundances of ^{148}Sm and ^{150}Sm are strongly affected by branchings at ^{147}Nd, ^{148}Nd and ^{150}Nd. Once the branching nuclei capture the neutrons, they will bypass ^{148}Sm in the flow, and the ^{150}Sm abundance-times-cross section product will be larger for ^{150}Sm than for ^{148}Sm. Considering that the n-capture rate $\lambda_{\rm n}$ is proportional to the neutron density $n_{\rm n}$, $n_{\rm n}$ can be evaluated from the relative ^{150}Sm ^{148}Sm abundances, resulting in $n_{\rm n} = (4.1 \pm 0.6) \times 10^8$ cm^{-3} [30]. Similarly, the weak s-process component (produced in the He- and C-burning phases of massive stars) yields neutron densities of order $(0.5 - 1.3) \times 10^8$ cm^{-3} [31, 32].

The temperature of the s-process sites can be determined by the dependence of nuclear states population on temperature at the branchings. It is important to note that under stellar conditions, the β-half-lives can significantly differ from the laboratory values. In the laboratory, only the ground state of the nucleus decays. However, the nuclear excited

states are thermally populated depending on the temperature in the astrophysical sites. If these excited states have significantly different lifetimes compared to the lifetime of the ground state, the stellar beta decay rate of a nucleus can deviate from the laboratory value. In addition, the branching ratio of the *s*-process flux reflects the the competition of n-capture and beta decay rates. Combining these two facts, *s*-process abundances at branching points allow us to determine the temperature of the *s*-process site in stars [25]. For example, according to the research on ^{176}Lu branching [33], the *s*-process occurs at the temperature $T = (2.5 - 3.5) \times 10^8$ K. More results from various branching analyses of relevance are found in Table 2.1.

Branch point isotope	Deduced *s*-process parameter	Reference
^{147}Nd/^{147}Pm/^{148}Pm	$n_{\rm n} = (4.1 \pm 0.6) \times 10^8$ cm^{-3}	[34]
^{151}Sm/^{154}Eu	$T = (3.5 \pm 0.4) \times 10^8$ K	[35]
^{163}Dy/^{163}Ho	$\rho = (6.5 \pm 3.5) \times 10^3$ g·cm^{-3}	[36]
^{176}Lu	$T = (3.1 \pm 0.6) \times 10^8$ K	[33, 37]
^{121}Sn/^{122}Sb	$T > 2.4 \times 10^8$ K	[38]
^{134}Cs	$T = (1.9 \pm 0.3) \times 10^8$ K	[39]
	$T = (1.7 \pm 0.5) \times 10^8$ K	[40]
^{185}W/^{186}Re	$n_{\rm n} = (3.5^{+1.7}_{-1.1}) \times 10^8$ cm^{-3}	[41]

Table 2.1: The *s*-process parameters from various branching analyses of relevance for the main *s*-process component (taken from Ref. [26]).

2.1.2 The r-process

Many n-capture isotopes are produced exclusively by the *s*-process or the *r*-process or, some by both processes as shown in Fig. 2.3. The two processes contribute roughly equally to the nucleosynthesis of heavy isotopes. The basic ideas of the *r*-process have been known for some time, however, we still do not know where exactly the *r*-process occurs and what the reaction sequence is. Considering the density of free neutrons required for the *r*-process, the *r*-process sites point to explosive environments. Supernovae have long been the prime suspects. Some early studies suggested the edge of the collapsing core of a type II supernova as the site of the *r*-process [1, 2]. But many difficulties arose in actual confirmation because it was difficult to create realistic supernova models that yield explosions. Fortunately, the situation has been improving rapidly with new high-resolution abundance observations of n-capture elements and models of core-collapse supernovae.

The most important feature of the *r*-process is that a large flux of neutrons becomes available in a short time interval for addition to elements of the iron group. The precise source of neutrons is not an important issue in this work; any source capable of supplying a large neutron flux on a time-scale of order 10-100 seconds, would meet the *r*-process requirements. The possible astrophysical sites for the *r*-process could be at the neutron

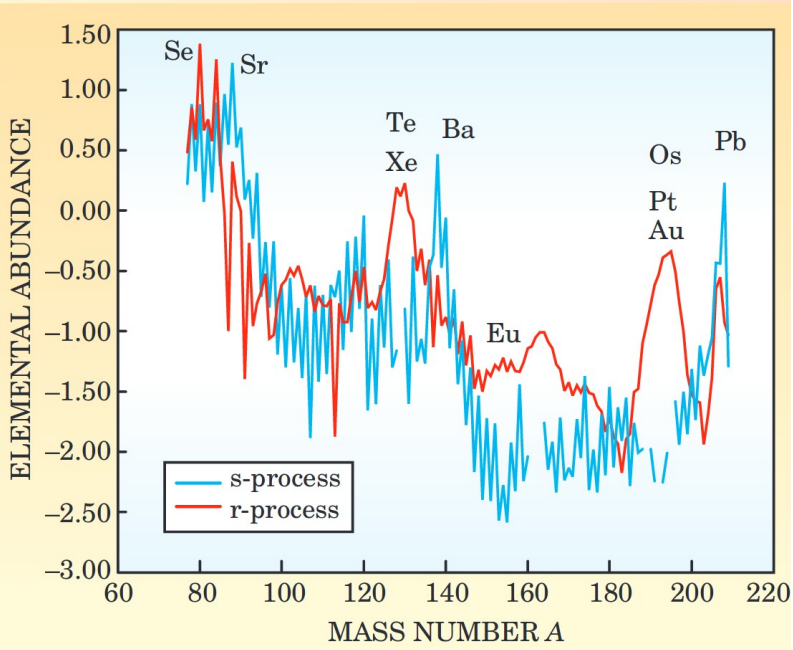

Figure 2.3: Solar system abundances of heavy elements produced by r- and s- processes. Plotted values are the s- and p- nuclei abundances relative to hydrogen. The curves are not normalised; the two processes have approximately the same contribution to the solar system's inventory of heavy elements (taken from Refs. [1, 24]).

number density $n_{\mathrm{n}} \approx 10^{24}$ cm^{-3} which might be reached in supernova envelopes at temperatures $T \approx 10^{9}$ K [2].

2.2 Physical sites and conditions of neutron capture processes

As introduced in Sec. 2.1, the astrophysical sites of the s-process are mainly in the He-burning layers of low-mass asymptotic giant branch (AGB) stars [28]. While astrophysical sites of the r-process are not yet unambiguously recognised, the s-process will be the main focus of this work. And for the further research, first, we have to choose physical parameters to describe our stellar plasmas in the neutron capture nucleosynthesis. Determination of parameters will be discussed in this Section in detail following the Section 2.4 of Ref. [3] and Ref. [42].

AGB stars are the final evolution stage of low- and intermediate-mass stars (up to about $8M_{\odot}$ [solar mass]) driven by nuclear burning. This phase is characterised by nuclear burning of H and He in thin shells on top of the electron-degenerate core of C and O as depicted in Fig. 2.4 [43]. During the AGB, the H shell dominates the

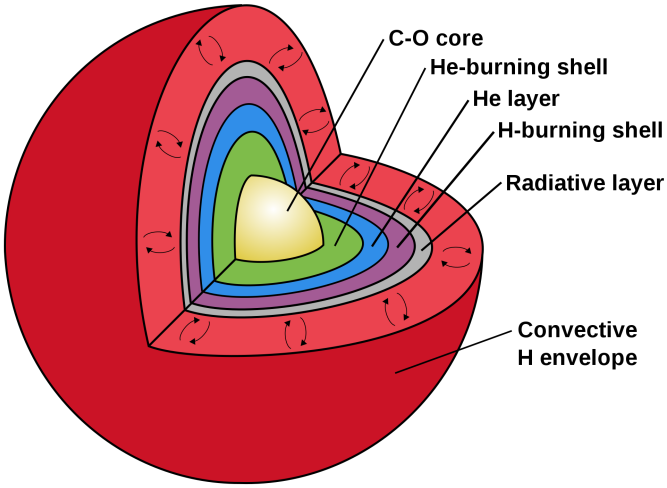

Figure 2.4: Schematic structure of an AGB star (taken from Ref. [44]). The stellar structure consists of a degenerate C-O core, the He-burning shell, a thin (10^{-2} to $10^{-3} M_{\odot}$) zone between the H shell and the He shell (He intershell), the H-burning shell, and a large convective envelope [42].

energy production for most of the time. H is transformed into He. Consequently, the He shell (hereafter He intershell) expands and is progressively compressed and heated until the temperature and density become high enough that He burning is triggered in the bottom layers. The thermonuclear runaway, i.e., *thermal pulse*, generated by this sudden release of energy makes most of the He intershell becoming convective, while the envelope expands and the H shell cools down, the convective He intershell is also recognised as *pulse-driven convective zone* (PDCZ). Within the PDCZ, partial He burning creates large amounts of C. The PDCZ quenches after a time of a few tens to a few hundreds of years, meanwhile, He burning continues radiatively for another few thousand years, and the H shell is inactive. The the envelope contracts and H shell burning starts again. The cycle is repeated for a few up to possibly 100 times. After a limited number of thermal pulses, the convective envelope penetrates the top layers of the He intershell, bringing the surface newly synthesised He, C and elements produced by neutron captures. This recurrent phenomenon is called *third dredge-up* (TDU) and the C left behind in the envelope is called ^{13}C pocket. Protons in the envelope are captured by ^{12}C and undergo the sequence ^{12}C(p,γ)^{13}Ne(β^{+},ν)^{13}C, which finally forms the ^{13}C pocket as shown in Fig. 2.5. Consecutively, the sequence ^{13}C(α,n)^{16}O provides a slow but sufficiently high neutron flux for the *s*-process nucleosynthesis [45]. This sequence starts at a temperature of about $T \sim 0.9 \times 10^{8}$ K. When the temperature exceeds 2.7×10^{8} K, another source of free neutrons will be available via ^{22}Ne(α,n)^{25}Mg reaction.

Based on these facts, for the *s*-process physical site, we will mainly refer to the C pocket site in this work. The pocket mass is a uniform mixture of C (20-25%), He (73-

78%) and a small amount of O [46]. Thus, the considered stellar plasmas will mostly be composed of He, C with some H mixed from the convective envelope and a few negligible heavier elements formed by the *s*-process. The chosen plasma compositions are shown in Table 2.2. For the temperature, we select $T_1 = 0.9 \times 10^8$ K in which the required free neutron flux is reached for the first time, and $T_2 = 3.48 \times 10^8$ K (≈ 30 keV), the widely used *s*-process temperature condition according to the classical *s*-process model.

Elements	H	He	C	O
Composition 1	-	78%	20%	2%
Composition 2	75%	25%	-	-

Table 2.2: Chosen plasma compositions for the *s*-process physical sites. The percentages are in terms of mass fractions.

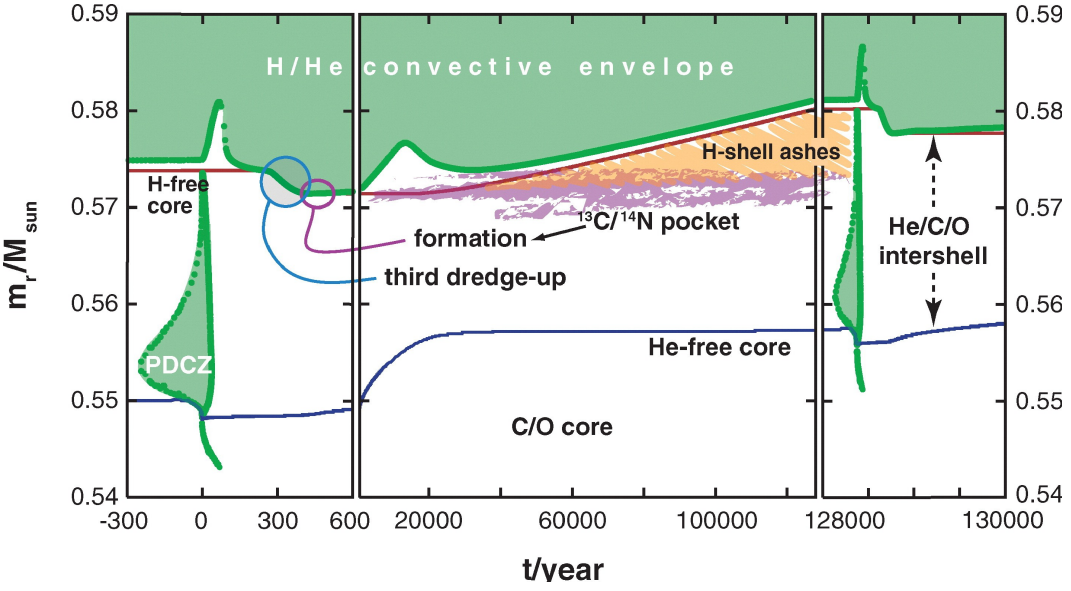

Figure 2.5: Illustration of the mass region during the time t of two thermal pulses and their interpulse phase for a low-mass AGB star. The red solid line indicates the mass coordinate of the H-free core. The dotted green line shows the boundaries of convection; each dot corresponds to one model in time. Convection zones are light green. The shown section of the evolution comprises 12,000 time steps. The colours indicate convection zones, layers with H-shell ashes and the region of the ^{13}C pocket (taken from Ref. [43]).

Chapter 3

Local Thermodynamic Equilibrium

3.1 LTE assumption

So far, we have introduced the astrophysical sites of interest in Sec. 2.1. Some physical parameters (such as temperature, neutron density and matter density) describing the nucleosynthesis sites are given also in Subsec. 2.1.1 and 2.1.2. According to present knowledge, the s-process is expected to take place at the temperature $T \approx 3.5 \times 10^8$K and the neutron density $n_{\rm n} \approx 10^8 {\rm cm}^{-3}$; the r-process site is expected to be at the temperature $T \approx 10^9$K and at the neutron density $n_{\rm n} \approx 10^{24} {\rm cm}^{-3}$. From those parameters, we can reasonably assume a hot and dense plasma environment for the nuclear reactions of interest. Now the question is how we describe such a hot and dense plasma, mostly in stars. To this end, we consider that the conditions of our plasma can be represented, *locally*, by the ideal condition of thermodynamic equilibrium. Thermodynamic equilibrium is interpreted as implying *thermal* equilibrium and ionisation-excitation equilibrium, but not necessarily nuclear equilibrium [47]. This point will be discussed in detail in the next Section following Chapters 3 and 4 of Ref. [47]. With the LTE assumption, the charge states of nuclei in our plasma can be simply described by the Saha ionisation equation in Sec. 3.2. Finally, the formalism of LTE will be discussed for generic nuclear two- and three- level systems in Sec. 3.3.

3.1.1 Thermal equilibrium

First we examine how well the thermal equilibrium requirement is satisfied in a nucleosynthesis site. Since thermal equilibrium is characterised by a common, uniform temperature in a given system, the examination of thermal equilibrium can be done by calculating the temperature gradient. We estimate the average temperature gradient in a AGB star (a s-process site, see Subsec. 2.1.1), for instance, by taking the 3×10^8 K for the central temperature $T_{\rm c}$ and $R \approx 10^2 L_\odot$ [solar radius] for the radius of the AGB star; we obtain

$$\left| \frac{dT}{dr} \right| \approx \frac{T_{\rm c}}{R} \approx 10^{-3} {\rm K/m}, \tag{3.1}$$

or equivalently, 1 K in 10^3 m. This is an extremely small temperature gradient. Furthermore, the opacity, i.e., the coupling between matter and radiation, of stellar material is typically so great that direct radiation from the source will arrive at a target in 10^{-3} m which corresponds to a few photon mean free paths. Thus as far as direct radiation is concerned, the material in a neighbourhood having a radius of a few photon mean free

paths will be shielded, i.e., the photon-photon interactions are dominant over the photon-particle interactions. In the same manner, under comparable conditions, the mean free path for collisions of an atom or ion with other particles, especially electrons, is generally orders of magnitude smaller than the photon mean free path. Again, the material in such a neighbourhood will be effectively shielded from the surroundings.

Taking the above considerations into account, the material in the vicinity of a given point is considered to be adiabatically enclosed and at constant temperature. In other words, the material is effectively in thermal equilibrium at the local temperature in the vicinity of any given point.

3.1.2 Ionisation-excitation equilibrium

Concerning the ionisation-excitation equilibrium of thermal equilibrium, the "reaction times" for ionisation and excitation processes can roughly be taken from the mean time between successive encounters of an atom or ion with photons or other particles; under typical stellar interior conditions, the reaction times are less than one second in most cases and are small compared with most time scales of astrophysical interest. Therefore, the ionisation-excitation equilibrium requirement appears to be well satisfied at a fixed point in the stellar interior. Together with the thermal equilibrium conditions described above, it is reasonable to suppose our astrophysical sites to reach, locally, thermodynamic equilibrium. Under the thermodynamic equilibrium condition, ionisation states in the system will follow the Maxwell-Boltzmann distribution. Therefore, the relative number densities of charge states of an ion in thermodynamic equilibrium can be simply calculated—by so-called Saha equation. We introduce the Saha equation in Section 3.2. The charge state distribution in the considered plasma will be calculated by solving the Saha equation.

3.1.3 Nuclear equilibrium

The strict thermodynamic equilibrium includes both thermal equilibrium and chemical equilibrium. However, this is only an idealised condition. In reality, systems can only be considered as being in *approximate* thermodynamic equilibrium and references to thermodynamic equilibrium are valid only in the context of the certain physical system under consideration and of the time scales of interest. As discussed already in 3.1.1 and 3.1.2, our system is considered to fulfill thermal equilibrium and partial chemical equilibrium for ionisation-excitation processes.

There are various chemical reactions possible in nature, each kind having its on reaction time t_{react} which is generally a function of matter density and temperature. To examine how well the system is in chemical equilibrium, we can compare the reaction relaxation time t_{react} of a specific chemical reaction, i.e., the characteristic time required for attaining chemical equilibrium for a certain reaction, with the time of interest t_{int}. If $t_{\mathrm{int}} > t_{\mathrm{react}}$, the chemical equilibrium is attained, and if $t_{\mathrm{int}} < t_{\mathrm{react}}$, chemical equilibrium is not established in the time of interest.

In applications to stars, the times of interest are generally long (say, for $T > 10^3$K) compared with the reaction times for chemical reactions involving molecules and for excitation and ionisation reactions involving molecules, atoms, ions, electrons, and photons. Equivalently, $t_{\rm int} > t_{\rm react}$, the chemical equilibrium is reached among molecules, atoms, ions, electrons, and photons. However, under stellar conditions in hotter environments (say, for $T < 10^9$K), these times of interest are becoming shorter compared with the time required for reaching chemical equilibrium among nuclei, i.e., $t_{\rm int} < t_{\rm react}$, thus nuclear reactions are not in equilibrium. For even larger temperatures, say, $T > 10^9$K, $t_{\rm int} \geq t_{\rm react}$. Considering that astrophysical sites of s- and r- processes are at the temperature of order $10^8 \sim 10^9$K, our system is mostly not in nuclear equilibrium.

In stellar work, a suitable interpretation of thermodynamic equilibrium is one that implies thermal equilibrium and chemical equilibrium among molecules, atoms, ions, electrons and photons, but not necessarily among nuclei. Thus, for example, a system in thermal equilibrium and in excitation-ionisation equilibrium, but in which irreversible nuclear reactions occur at a significant rate, would be still regarded as being in local thermodynamic equilibrium (LTE).

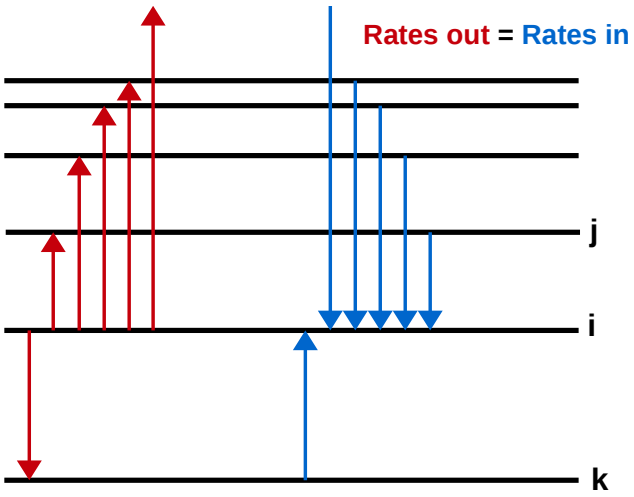

Figure 3.1: Illustration of the principle of detailed balancing for a level i in an atom. The sum of the rates of all transitions into a level i is balanced by the sum of the rates out (adapted from Ref. [48]), i.e., the net flow is zero. Moreover, each flow into individual energy level is balanced by its inverse.

Under the assumption of LTE, the material particles in the plasma are assumed to be in states that can be characterised by a single parameter, the temperature. Under these conditions, the populations of energy levels of atoms follow the Maxwell-Boltzmann statistics. The level populations are constant in time. Thus, the flow into any energy level must be balanced by the flow out of that level. This condition must hold at any time. However, in thermodynamic equilibrium, not only must the net flow be zero, so must the net flows that arise from individual levels as illustrated in Fig. 3.1. Every process must

be matched by its reciprocal process. This concept is known as the *principle of detailed balancing* [49]. This principle should hold as long as the system is in thermodynamic equilibrium.

However, in LTE, the system is not necessarily in nuclear equilibrium. In other words, the nuclear excited states possibly do not follow the standard Maxwell-Boltzmann distribution. For example, nuclear isomers, i.e., long-lived excited nuclear states, might prevent nuclear excited states populations to obey the Maxwell-Boltzmann distribution. The reason for this is that isomers can be directly populated by gamma decay cascades following neutron capture and can have beta decay rates very different from the ones of the nuclear ground states. Due to their long lifetime, equilibration with the ground state and the other non-isomeric excited states is not always possible. Therefore, isomers have to be treated as special nuclear species in the nucleosynthesis nuclear reaction networks under stellar conditions.

3.2 Saha ionisation equation

Under the assumption of LTE, we can use the Saha ionisation equation to describe the charge states of atoms in the plasma. The Saha equation which has been originally introduced by Megh Nad Saha in Ref. [21] gives us a clue about the charge state of an atom in the plasma. It provides us the relative number densities of the different charge states of specific atom species in thermodynamic equilibrium. In this Subsection, the Saha ionisation equation will be derived following the Chapter 3 of Refs. [3, 47].

From statistical mechanics [50], we know that, in thermodynamic equilibrium, the number of weakly interacting particles with total energies per particle in the range between E and $E + dE$ is given as

$$\begin{aligned} dN &= \frac{db}{\exp\left(E/k_BT - \eta\right) + 1} \quad \text{for fermions} \\ &= \frac{db}{\exp\left(E/k_BT - \eta\right) - 1} \quad \text{for bosons,} \end{aligned} \tag{3.2}$$

where db is the number of possible quantum states, η is the degeneracy parameter which is related to the chemical potential μ by $\eta = \mu/(k_BT)$, where T is the temperature and k_B is the Boltzmann constant. The factor db is often called the *statistical weight*, since, apart from the factor in the denominator, the probability of finding a particle will be proportional to db. If the levels in the system are discrete, such as in an atom, db becomes b_i, the *degree of degeneracy*, or the total number of quantum states with energy E. For example, db of an atom whose total angular momentum quantum number is J is

$$b_i(J) = 2J + 1, \tag{3.3}$$

thus, for a free electron, whose spin is $1/2$, $b_e = 2 \cdot \frac{1}{2} + 1 = 2$.

On the other hand, free particles have continuous energy levels. For the sake of counting

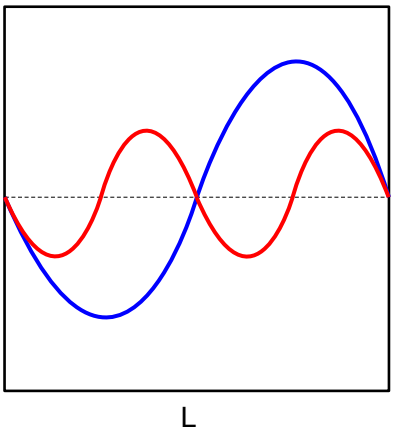

Figure 3.2: Standing waves in a box with sides L (adapted from Ref. [47]).

the number of quantum states in a given energy range, we confine the particles within a box of volume L^3. The de Brogile wavelength of the particle is

$$\lambda = h/p \tag{3.4}$$

where h is the Planck's constant and p is the momentum of the particle. Now λ can only have the values corresponding to standing waves, because the waves should have nodes on the boundaries. To have complete standing waves within the box, we must have the periodic boundary conditions

$$L = n_{x,y,z} \cdot \lambda_{x,y,z}, \quad n_{x,y,z} = 1, 2, \cdots, \tag{3.5}$$

or,

$$\lambda_{x,y,z} = L/n_{x,y,z} = h/p_{x,y,z} \tag{3.6}$$

for each direction (x, y, z), where

$$p_{x,y,z} = n_{x,y,z}h/L, \quad n_{x,y,z} = \pm 1, \pm 2, \cdots, \tag{3.7}$$

where all negative values of $n_{x,y,z}$ are related to the negative values of $p_{x,y,z}$. Hence, the momenta of particles in the box can only have the discrete values

$$p^2 = \frac{h^2}{L^2}(n_x^2 + n_y^2 + n_z^2), \quad n_{x,y,z} = \pm 1, \pm 2, \cdots. \tag{3.8}$$

In the next step, we consider a box in *momentum space*, placing its corner at the origin, having sides of length $n_x h/L$, $n_y h/L$ and $n_z h/L$ as shown in Fig. 3.3. The number of lattice points, or equivalently, quantum states, contained therein is

$$(n_x + 1)(n_y + 1)(n_z + 1) \tag{3.9}$$

and the volume of the box in the momentum space is

$$n_x n_y n_z \frac{h^3}{L^3}. \tag{3.10}$$

Therefore, the number of quantum states per unit volume of momentum space is obtained

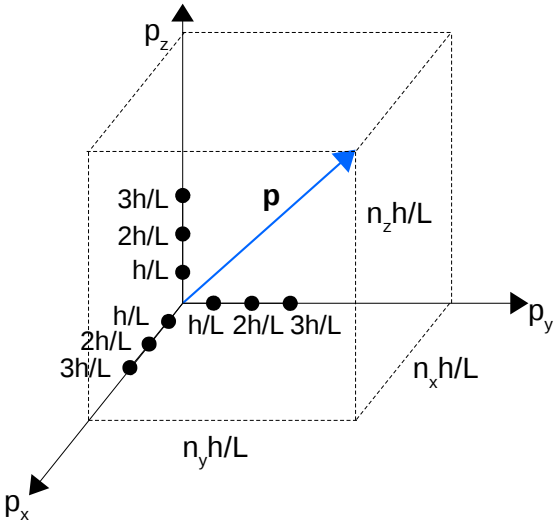

Figure 3.3: Momentum p of a particle in momentum space (adapted from Ref. [47]).

by dividing Eq. (3.9) by Eq. (3.10),

$$\left(1+\frac{1}{n_x}\right)\left(1+\frac{1}{n_y}\right)\left(1+\frac{1}{n_z}\right)\frac{L^3}{h^3} \simeq \frac{L^3}{h^3}, \tag{3.11}$$

if we take $n_{x,y,z}$ sufficiently large. This gives a volume of h^3 per particle in phase space. With the phase space volume $Vp^2dpd\Omega$ (particles confined in solid angle Ω with momenta between p and $p+dp$), the statistical weight of free particles within the full solid angle will be

$$db = \frac{4\pi p^2 dp}{h^3} V. \tag{3.12}$$

As long as electrons can occupy the same quantum state twice with different spins as stated in Pauli's exclusion principle, we multiply the factor 2 to the obtained statistical weight b_e. Putting the above equations together, we can calculate the number density of electrons with energy E_e from Eq. (3.2):

$$n_e = \frac{N}{V} = b_e \int_0^\infty \frac{dN}{V} = b_e \int_0^\infty \frac{4\pi p^2 dp}{h^3} \frac{1}{\exp\left[E_e/k_B T - \eta\right] + 1}. \tag{3.13}$$

Now we focus on non-degenerate particles with the constraint $-\eta \gg 1$, corresponding to a specific ionisation state and in a discrete state k. Then Eq. (3.2) reduces to the

Maxwell-Boltzmann distribution

$$N_k = b_k \exp\left[\eta - \epsilon_k / k_B T\right], \tag{3.14}$$

where ϵ_k is the excitation potential. The ratio between two excitation levels k and o returns the *Boltzmann equation*:

$$\frac{N_k}{N_o} = \frac{b_k}{b_o} \exp\left[(\epsilon_o - \epsilon_k)/k_B T\right]. \tag{3.15}$$

Our system is composed of a mixture of particles of three kinds:

(1) j-times ionised atoms (i.e., an atom has lost j electrons) of a kind;
(2) $(j+1)$-times ionised atoms of the same kind;
(3) free electrons.

For the particle types of (1) and (2), only the total numbers of ions for the given ionisation state is considered and they are assumed to be non-degenerate ($-\eta_{j+1} \gg 1$ and $-\eta_j \gg 1$) and non-relativistic. Under the chemical equilibrium condition, every reaction will happen at the same rate as its reverse reaction. This can be expressed as an equation with the chemical potential μ. For our ionisation process,

$$\mu_{j+1} + \mu_e - \mu_j = 0, \tag{3.16}$$

with the μ_{j+1} indicating the chemical potential of the $(j+1)$-times ionised atom and the subscript e denoting the electron. Assuming identical temperature for each reactant, and using the definition of degeneracy parameter, we have

$$\eta_j = \eta_{j+1} + \eta_e, \tag{3.17}$$

as the condition for chemical equilibrium. The corresponding energies for particles are,

$$\begin{aligned}
&\text{particle (1)} : E_{i,j,k} = \frac{p_1^2}{2m_{i,j}} + \epsilon_{i,j,k}, \\
&\text{particle (2)} : E_{i,j+1,o} = \frac{p_2^2}{2m_{i,j+1}} + \epsilon_{i,j+1,o} + I_{i,j} - m_e c^2, \\
&\text{particle (3)} : E_e,
\end{aligned} \tag{3.18}$$

where $I_{i,j}$ is the ionisation potential of an atom of species i in ionisation state j the minimum energy required to remove an electron from the ground state of j-times ionised atom; $\epsilon_{i,j,k}$ is the excitation potential of the excited levels above the ground states of the given atom species with k denoting the excitation state, and m is the mass of a given particle. Here, $I_{i,j}$ does not consider the mass loss of the atom from the ionisation, therefore, one has to subtract the electron rest energy from particle (2) by hand. As a result, E_e contains the kinetic and rest energy the electron.
To finally get the number density for particle (1) and (2), one has to know the number

of occupied quantum states. This can be done by summing over the statistical weights per energy level weighted by the Boltzmann factor which is equivalent to the partition function

$$b_{i,j} = \sum_k b_{i,j,k} \exp\left(-\frac{\epsilon_{i,j,k}}{k_B T}\right). \tag{3.19}$$

Combining Eqs. (3.18), (3.19) and the non-degenerate condition $-\eta \gg 1$ and using Eq. (3.16), the number densities for particle (1) and (2) are

$$\begin{aligned} &\text{particle (1): } n_{i,j} = b_{i,j} e^{\frac{\mu_{i,j+1}+\mu_e}{k_B T}} \int_0^\infty \frac{4\pi p^2 dp}{h^3} e^{-\frac{p_1^2}{2m_{i,j}k_B T}}, \\ &\text{particle (2): } n_{i,j+1} = b_{i,j+1} e^{\frac{\mu_{i,j+1}}{k_B T}+\frac{m_e c^2}{k_B T}-\frac{I_{i,j}}{k_B T}} \int_0^\infty \frac{4\pi p^2 dp}{h^3} e^{-\frac{p_1^2}{2m_{i,j}k_B T}}. \end{aligned} \tag{3.20}$$

Integrating over p, we obtain

$$\begin{aligned} n_{i,j} &= b_{i,j} e^{\frac{\mu_{i,j+1}+\mu_e}{k_B T}} \frac{(2\pi m_{i,j} k_B T)^{3/2}}{h^3}, \\ n_{i,j+1} &= b_{i,j+1} e^{\frac{\mu_{i,j+1}}{k_B T}+\frac{m_e c^2}{k_B T}-\frac{I_{i,j}}{k_B T}} \frac{(2\pi m_{i,j+1} k_B T)^{3/2}}{h^3}. \end{aligned} \tag{3.21}$$

Finally, we divide $n_{i,j}$ by $n_{i,j+1}$ to obtain the Saha equation:

$$\frac{n_{i,j+1}}{n_{i,j}} = \frac{b_{i,j+1}}{b_{i,j}} \cdot \left(\frac{m_{i,j+1}}{m_{i,j}}\right)^{3/2} \cdot \exp\left(\frac{m_e c^2}{k_B T} - \frac{I_{i,j}}{k_B T} - \frac{\mu_e}{k_B T}\right). \tag{3.22}$$

3.3 Internal nuclear equilibration

Generally, the discussions of s-process branchings [11, 51, 52] have been based on the fact that, for the time-scale determining species, the branching is completely dependent on the competition between neutron capture and excited state beta decay. And this assumed that in thermodynamic equilibrium, all branching nuclei are fractionally distributed among their excited states according to the Boltzmann statistical factors. However, this assumption is valid only if the de-excitations of all excited states to their ground states by radiative decays happen on a shorter time scale than ones via beta decay. Therefore, one has to investigate the conditions for reaching this "thermodynamic equilibrium". Many important nuclei in s-process branchings have long-lived isomeric states that are directly populated by either neutron capture from the previous isotope or by beta decay from the parent isobar. And such long-lived isomeric states are likely to influence the nucleosynthesis paths. For example, for these long-lived isomeric states, there is a significant beta decay branching directly to the next isobar because the state's spontaneous radiative de-excitation to the ground state is slower compared to the state's beta decay. Or alternatively, if the lifetime of the isomeric state is even longer than that of the ground state, then it might capture neutrons itself and thereby it results in a significant fraction of the total s-process neutron-capture current to pass on through to the

next isotope, instead of the flow proceeding totally through the ground state's fast beta decay to the next isobar [8]. In this Section, we introduce simple two-level and three-level system formalisms to estimate the time scale of the internal nuclear equilibration, in a way that we can quantitatively compare the equilibration time scale of different nuclear processes within isomers. Further, we applying these formalisms to the stellar conditions where the NEEC and IC are happening to examine the impact of the NEEC and IC processes in thermalisation.

In this Section, the internal nuclear equilibration by simple two-level and three-level system will be quantitatively introduced by following the Sections II and III of Ref. [14]. This discussion is mainly aiming to obtain the relevant time scales as a function of stellar temperature to establish a thermal distribution of excited-state populations. These internal equilibration times will be compared with other time scales of interest and finally in order to confirm whether or not the isomer and the ground state have sufficient time to obtain thermal equilibrium.

3.3.1 Two-level system

The internal equilibration processes of a two-level system are illustrated in Fig. 3.4. An idealised nucleus which has only a ground state (o) and a single excited state (e) has various production (po and pe), internal equilibration (oe and eo) and destruction (od and ed) channels. Each state is first produced by the production rates as shown in Fig. 3.4, and goes through the de-excitation and destruction processes with the corresponding rates. All rates (s^{-1}) are given with appropriate subscripts and g ($= 2J + 1$) is the statistical factor for each state.
The time evolution of the abundances n_o and n_e (cm^{-3}) of the ground and excited states can be described as follows

$$\begin{aligned} \frac{dn_o}{dt} &= \lambda_{po} n_p - (\lambda_{oe} + \lambda_{od}) n_o + \lambda_{eo} n_e, \\ \frac{dn_e}{dt} &= \lambda_{pe} n_p - (\lambda_{eo} + \lambda_{ed}) n_e + \lambda_{oe} n_o. \end{aligned} \tag{3.23}$$

The above Eq. (3.23) can be easily solved if one assumes the zero production source abundance, $n_p = 0$ and all other rates to be positive constants. Then the Eq. (3.23) gives the time-dependent solution

$$\begin{aligned} n_o(t) =& \frac{n_p}{s_1 s_2} [\lambda_{eo}(\lambda_{po} + \lambda_{pe}) + \lambda_{ed}\lambda_{po}] + \\ & \frac{n_p}{s_2 - s_1} \sum_{j=1}^{2} \frac{(-1)^j}{s_j} e^{s_j t} [\lambda_{po}(s_j + \lambda_{eo} + \lambda_{ed}) + \lambda_{pe}\lambda_{eo}], \end{aligned} \tag{3.24}$$

where s_1 and s_2 are the two negative solutions of the quadratic polynomial

$$Q(s) \equiv s^2 + (\lambda_{eo} + \lambda_{oe} + \lambda_{ed} + \lambda_{od}) s + \lambda_{od}(\lambda_{eo} + \lambda_{ed}) + \lambda_{oe}\lambda_{ed}. \tag{3.25}$$

This time-dependent solution of the ground state abundance determines how fast internal equilibration operates.

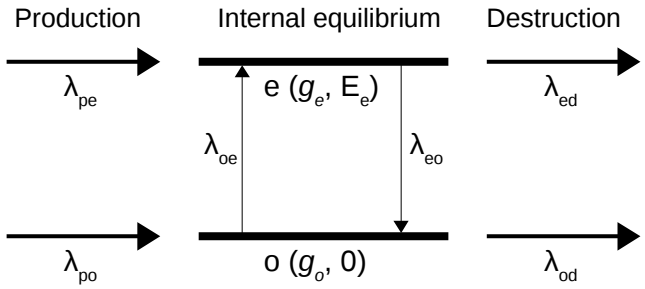

Figure 3.4: The internal equilibration of a two-level system. A single excited state and the ground state of a nucleus are connected by internal rates λ_{oe} and λ_{eo}. Arrows give the direction of the flows into and out of the ground state (which is indicated by o, at ground energy 0 with statistical factor g_o) and the excited state (which is indicated by e, at excitation energy E_e with statistical factor g_e). Each level is produced at the rate λ_{pk} ($k = o, e$) and is destroyed at the rate λ_{kd} (adapted from Ref. [14].

Using the property that Eqs. (3.23) and (3.25) are symmetric under interchanging o and e, one can easily obtain the solution for $n_e(t)$ by the substitutions $o \rightleftharpoons e$. Combining Eq. (3.24) and the analogous solution of $n_e(t)$, it is clear that the ratio $n_e(t)/n_o(t)$ depends on the production branching ratios

$$f_{po} = 1 - f_{pe} \equiv \frac{\lambda_{po}}{\lambda_{po} + \lambda_{pe}}. \tag{3.26}$$

From Eq. (3.24), one can take the steady-state limit with $t \to \infty$, which gives

$$\left(\frac{n_e}{n_o}\right)_{t\to\infty} = \frac{\lambda_{oe} + f_{pe}\lambda_{od}}{\lambda_{eo} + f_{po}\lambda_{ed}}. \tag{3.27}$$

For isomeric nuclear excited states, the production and the destruction rates are generally faster compared to the internal equilibration rates, as a result, the rapid destruction is possible, i.e., $f_{pe}\lambda_{od} \gg \lambda_{oe}$ and $f_{po}\lambda_{ed} \gg \lambda_{eo}$. Therefore, in Eq. (3.27), the steady-state abundance ratio becomes

$$\left(\frac{n_e}{n_o}\right)_{t\to\infty} = \frac{f_{pe}\lambda_{od}}{f_{po}\lambda_{ed}}. \tag{3.28}$$

For non-isomeric nuclear excited states, it is generally the case that $\lambda_{eo} \gg \lambda_{ed}$, since the typical lifetimes of such excited states are on the order of nanoseconds to picoseconds. This exactly means that non-isomeric nuclear excited states are rather de-excited to the ground state than are destroyed to other nuclear species. Considering that the upward

transition rate from the ground state to the excited state λ_{oe} is retarded compared to λ_{eo} by the Boltzmann factor as

$$\lambda_{oe} = \lambda_{eo} \left(\frac{g_e}{g_o} \right) \exp \left(\frac{-E_e}{k_B T} \right), \tag{3.29}$$

which means that $\lambda_{oe} \ll f_{pe}\lambda_{od}$ is mostly true even for non-isomeric cases. Applying the above general characteristics of nuclear states, $\lambda_{eo} \gg \lambda_{ed}$ and $\lambda_{oe} \ll f_{pe}\lambda_{od}$ to Eq.(3.27), the ratio becomes

$$\left(\frac{n_e}{n_o} \right)_{t\to\infty} = \frac{f_{pe}\lambda_{od}}{\lambda_{eo}} = \left(\frac{f_{pe}\lambda_{od}}{\lambda_{oe}} \right) \left(\frac{\lambda_{oe}}{\lambda_{eo}} \right) \gg \left(\frac{\lambda_{oe}}{\lambda_{eo}} \right). \tag{3.30}$$

This ratio can be compared with the thermal population ratio under zero nuclear destruction assumption, i.e., $\lambda_{od} = \lambda_{ed} \to 0$. And Eq. (3.25) becomes

$$Q(s) = s^2 + (\lambda_{eo} + \lambda_{oe})s \tag{3.31}$$

and the time-dependent solution of the ground state abundance is

$$n_o(t) = \frac{n_p \lambda_{eo}(\lambda_{po} + \lambda_{pe})t}{\lambda_{eo} + \lambda_{oe}} + n_p \frac{\lambda_{pe}\lambda_{eo} - \lambda_{po}\lambda_{oe}}{(\lambda_{eo} + \lambda_{oe})^2} \{\exp[-(\lambda_{eo} + \lambda_{oe})t] - 1\}. \tag{3.32}$$

Thus for small t, $n_o(t) \to n_p \lambda_{po} t$. An analogous solution of $n_e(t)$ is again obtained by interchanging o and e from Eq. (3.32) using the same technique which has already performed at the beginning of this Section to obtain the general solution of $n_e(t)$.

Applying the zero destruction assumption to Eq. (3.27) and using the relation between λ_{oe} and λ_{eo} in Eq. (3.29), the abundance ratio becomes

$$\left(\frac{n_e}{n_o} \right)_{t\to\infty} = \frac{\lambda_{oe}}{\lambda_{eo}} = \frac{g_e}{g_o} \exp \left(\frac{-E_e}{k_B T} \right). \tag{3.33}$$

Consequently, the steady-state abundance ratio with zero external destruction is exactly the thermal-equilibrium value for general non-isomeric nuclear states. Comparing the steady-state abundance ratio in Eq. (3.30) exceeds the thermal population ratio in Eq. (3.33). This equilibrium is achieved on a time scale

$$t \geq \tau_{eq} \equiv (\lambda_{oe} + \lambda_{eo})^{-1} = \frac{1/\lambda_{eo}}{1 + (g_e/g_o) \exp\left(-E_e/k_B T\right)}, \tag{3.34}$$

where τ_{eq} is the mean lifetime in the exponential term in Eq. (3.32). Assuming that the spontaneous electromagnetic transition rate λ^s_{eo} of the excited states is enhanced only by stimulated emission from the hot stellar photon bath, then the internal equilibration time of nucleus is given by

$$\tau_{eq} = \frac{1 - \exp\left(-E_e/k_BT\right)}{1 + (g_e/g_o)\exp\left(-E_e/k_BT\right)} \frac{1}{\lambda^s_{eo}} \tag{3.35}$$

$$\Rightarrow \frac{1}{\lambda^s_{eo}} \qquad \text{for } k_BT \ll E_e \tag{3.36}$$

$$\Rightarrow \frac{E_e/k_BT}{(1 + g_e/g_o)\lambda^s_{eo}} \qquad \text{for } k_BT \gg E_e \ . \tag{3.37}$$

From Eqs. (3.35), (3.36) and (3.37), it is evident that $\tau_{eq} \leq 1/\lambda^s_{eo}$ in all cases. In consequence, if there are no external destruction rates for the nuclear states, internal thermal equilibrium will be reached on a time scale of the downward spontaneous radiative transition lifetime or less than that [8, 53].
If one considers the case where states in simplified two-level system are destroyed by destruction rates λ_{od} and λ_{ed}, the total steady-state destruction rates, λ_{ss}, is defined as

$$\lambda_{ss} \equiv \frac{n_o(t \to \infty)\lambda_{od} + n_e(t \to \infty)\lambda_{ed}}{n_o(t \to \infty) + n_e(t \to \infty)} = \frac{\lambda_{od}(\lambda_{eo} + f_{po}\lambda_{ed}) + \lambda_{ed}(\lambda_{oe} + f_{pe}\lambda_{od})}{\lambda_{eo} + \lambda_{oe} + f_{po}\lambda_{ed} + f_{pe}\lambda_{od}}. \tag{3.38}$$

For the case of rapid internal equilibration, i.e., no nuclear destruction assumption, using Eq. (3.33), Eq. (3.38) reduces to

$$\lambda_{ss} = \frac{\lambda_{od} + (g_e/g_o)\exp\left(-E_e/k_BT\right)\lambda_{ed}}{1 + (g_e/g_o)\exp\left(-E_e/k_BT\right)}. \tag{3.39}$$

For the case of rapid nuclear destruction, i.e., the opposite of the former case, from Eq. (3.28), the total steady-state destruction rate becomes

$$\lambda_{ss} = \frac{\lambda_{ed}\lambda_{od}}{f_{po}\lambda_{ed} + f_{pe}\lambda_{od}}. \tag{3.40}$$

From Eqs, (3.39) and (3.40), one can conclude that if the destruction rates (λ_{od} and λ_{ed}) are sufficiently rapid, then the "stellar reaction rate λ_{ss}" is becoming considerable which implies a deviation from the normal thermal-mixture.
For some nuclei with sufficiently long isomeric states, their spontaneous radiative decays are not rapid enough (i.e., $\lambda_{eo} \leq \lambda_{ed}$) such that direct internal coupling to the ground state is not available. In the following Subsection, the indirect flows between the isomeric state and the ground state triggered via higher-lying intermediate state will be investigated.

3.3.2 Three-level system

In addition to the two-level formalism, now the simplest form of three-level system will be introduced. The prototype of three-level system is shown in Fig. 3.5. The system consists of the ground state o, the isomeric state m and higher-lying intermediate state i.

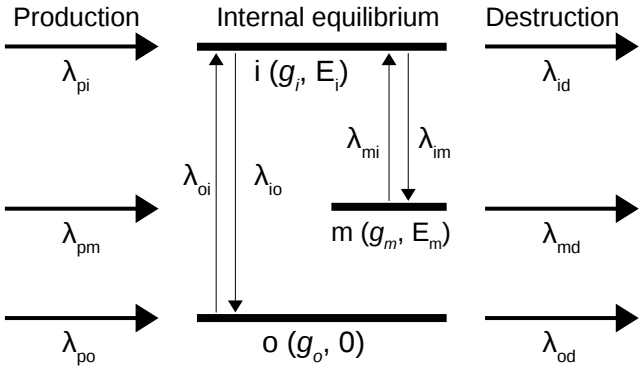

Figure 3.5: The internal equilibration of three-level system with no direct transition between isomeric states and the ground state. The format is the same as in Fig. 3.4 but for an additional isomeric state m between the ground state o and the high-lying excited state i. All the rates of interest are indicated with appropriate subscripts as in Fig. 3.4 (adapted from Ref. [14]).

The isomeric state m and the ground state o are not directly connected, but they are linked indirectly via the intermediate higher-lying state i. Each level is produced at the constant source production rate λ_{pk} $(k = i, m, o)$ and is destroyed at the constant destruction rate λ_{kd}. The time evolution of the abundances is given by the coupled differential equations

$$\begin{aligned}
\frac{dn_o}{dt} &= \lambda_{po} n_p - (\lambda_{oi} + \lambda_{od}) n_o + \lambda_{io} n_i, \\
\frac{dn_m}{dt} &= \lambda_{pm} n_p - (\lambda_{mi} + \lambda_{md}) n_m + \lambda_{im} n_i, \\
\frac{dn_i}{dt} &= \lambda_{pi} n_p - (\lambda_{io} + \lambda_{im} + \lambda_{id}) n_i + \lambda_{oi} n_o + \lambda_{mi} n_m.
\end{aligned} \tag{3.41}$$

Equations (3.41) are most simply solved, again, under the assumption that all the rates λ and the source abundance n_p are constant in time and all other abundances are initially set to be zero. The time-dependent solution of Equations (3.41) is given as

$$\begin{aligned}
n_o(t) &= \frac{-n_p}{s_1 s_2 s_3} \\
&\times \{[\lambda_{io}(\lambda_{po} + \lambda_{pm} + \lambda_{pi}) + \lambda_{po}\lambda_{id}]\lambda_{mi} + [\lambda_{po}(\lambda_{io} + \lambda_{im} + \lambda_{id}) + \lambda_{pi}\lambda_{io}]\lambda_{md}\} \\
&+ n_p \sum_{j=1}^{3} \frac{\exp(s_j t)}{s_j} \Big[\prod_{l=1, l\neq j}^{3} \frac{1}{(s_j - s_l)} \Big] \{[\lambda_{io}(\lambda_{po} + \lambda_{pm} + \lambda_{pi}) + \lambda_{po}(s_j + \lambda_{id})]\lambda_{mi} \\
&+ [\lambda_{po}(s_j + \lambda_{io} + \lambda_{im} + \lambda_{id}) + \lambda_{pi}\lambda_{io}](s_j + \lambda_{md})\},
\end{aligned} \tag{3.42}$$

where s_1, s_2 and s_3 are distinct negative roots of the polynomial

$$C(s) \equiv (s+\lambda_{io}+\lambda_{im}+\lambda_{id})(s+\lambda_{oi}+\lambda_{od})(s+\lambda_{mi}+\lambda_{md}) \\ -\lambda_{im}\lambda_{mi}(s+\lambda_{oi}+\lambda_{od})-\lambda_{io}\lambda_{oi}(s+\lambda_{mi}+\lambda_{md}). \tag{3.43}$$

Again, the analogous solution forthe isomeric state abundance, $n_m(t)$, can be obtained by interchanging the subscripts o and m. With the obtained solutions $n_o(t)$ and $n_e(t)$, one can examine the abundance ratio $n_o(t)/n_m(t)$. This ratio is independent of the constant total production rate, i.e., $(\lambda_{pi}+\lambda_{pm}+\lambda_{po})$, for all times.
Before introducing the steady-state abundance ratio as in Subsection 3.3.1, first, one defines the intermediate state branching ratio, as

$$f_{ia} \equiv \frac{\lambda_{ia}}{\lambda_{io}+\lambda_{im}+\lambda_{id}} \qquad \text{for } a = o, m, d, \tag{3.44}$$

and the source branching ratio, as

$$f_{pb} \equiv \frac{\lambda_{pb}}{\lambda_{po}+\lambda_{pm}+\lambda_{pi}} \qquad \text{for } b = o, m, i. \tag{3.45}$$

Since the first term in Eq. (3.42) indicates the steady state solution, it is easy to attain the steady-state abundance ratio,

$$\left(\frac{n_m}{n_o}\right)_{t\to\infty} = \frac{(f_{im}+f_{pm}f_{id})\lambda_{oi}+(f_{pm}+f_{pi}f_{im})\lambda_{od}}{(f_{io}+f_{po}f_{id})\lambda_{mi}+(f_{po}+f_{pi}f_{io})\lambda_{md}}. \tag{3.46}$$

Consider now the two extreme cases for Eq. (3.46). If the destruction rates are sufficiently rapid, then one obtains

$$\left(\frac{n_m}{n_o}\right)_{t\to\infty} = \frac{(f_{pm}+f_{pi}f_{im})\lambda_{od}}{(f_{po}+f_{pi}f_{io})\lambda_{md}}. \tag{3.47}$$

Or else, if the internal equilibration rates are dominant over the destruction rates, then one has

$$\left(\frac{n_m}{n_o}\right)_{t\to\infty} = \frac{f_{im}\lambda_{oi}}{f_{io}\lambda_{mi}} = \left(\frac{\lambda_{im}}{\lambda_{mi}}\right)\left(\frac{\lambda_{oi}}{\lambda_{io}}\right). \tag{3.48}$$

According to the principle of detailed balance, the thermal-equilibrium population ratios between the upward and downward transition rates are weighted by the Boltzmann factors, as

$$\frac{\lambda_{oi}}{\lambda_{io}} = \frac{g_i}{g_o}\exp\left(-E_i/k_BT\right) \tag{3.49}$$

and

$$\frac{\lambda_{mi}}{\lambda_{im}} = \frac{g_i}{g_m}\exp\left[-(E_i-E_m)/k_BT\right]. \tag{3.50}$$

Making use of Eqs. (3.49) and (3.50), Eq. (3.48) becomes

$$\left(\frac{n_m}{n_o}\right)_{t\to\infty} = \frac{g_m}{g_o}\exp\left(-E_m/k_BT\right). \tag{3.51}$$

The steady-state ratio is attained on a time scale which is determined by the roots of $C(s)$ in Eq. (3.43). The steady-state solution is achieved in times $t \gg 1/|s_3|$, where the three distinct roots of Eq. (3.43) are arrayed as $|s_3| > |s_2| > |s_1|$. To examine the time scale of the internal transition rates operating to produce the thermal equilibrium ratio in Eq. (3.51), one assumes zero destruction rates, i.e., $\lambda_{od} = \lambda_{md} = \lambda_{id} = 0$ and reexamines the polynomial $C(s)$ to find that $C(s) \to sR(s)$ where $R(s)$ is given as the polynomial

$$R(s) \equiv s^2 + \Lambda s + \Omega \tag{3.52}$$

with

$$\Lambda \equiv \lambda_{io} + \lambda_{oi} + \lambda_{im} + \lambda_{mi} \tag{3.53}$$

and

$$\Omega \equiv \lambda_{mi}\lambda_{io} + \lambda_{oi}(\lambda_{im} + \lambda_{mi}). \tag{3.54}$$

Here, we assume that the two distinct roots of $R(s)$ are given as

$$s_1 = \frac{-\Lambda - (\Lambda^2 - 4\Omega)^{1/2}}{2} \tag{3.55}$$

and

$$s_2 = \frac{-\Lambda + (\Lambda^2 - 4\Omega)^{1/2}}{2}. \tag{3.56}$$

To calculate the solution for zero nuclear destruction rates, we set $\lambda_{kd} = 0$, $k = o, m, d$ and the coupled Eq. (3.41) gives the solution

$$\begin{aligned} n_o(t) \Rightarrow \frac{n_p\lambda_{io}\lambda_{mi}(\lambda_{po} + \lambda_{pm} + \lambda_{pi})t}{s_1 s_2} + \frac{n_p}{s_2 - s_1}\sum_{j=1}^{2}\frac{(-1)^j}{s_j^2}[\exp\left(s_j t\right) - 1] \\ \times\{[\lambda_{io}(\lambda_{po} + \lambda_{pm} + \lambda_{pi})\lambda_{mi} + s_j[\lambda_{po}(\lambda_{io} + \lambda_{im} + \lambda_{mi}) + \lambda_{pi}\lambda_{io}] + \lambda_{po}s_j^2\}. \end{aligned} \tag{3.57}$$

The corresponding solution for $n_n(t)$ is attained by exchanging the subscripts o and m from Eq. (3.57) as it has been performed earlier. Since the destruction rates are neglected, in the steady-state limit where $t \to \infty$, n_m/n_o produces the thermal-equilibrium ratio of Eq. (3.48). The time scale of reaching this equilibrium is determined from s_1 and s_2. From Eqs. (3.49) and (3.50), it is clear that the upward transition rates are weighted by Boltzmann factors compared to the downward transition rates. Using this property, we can take $\lambda_{oi} \ll \lambda_{io}$ and $\lambda_{mi} \ll \lambda_{im}$ for our estimation. Additionally, we can easily get that $\Lambda^2 \gg 4\Omega$. Combining these and expanding the second term, the roots of $R(s)$ then become

$$s_1 \approx -\Lambda \approx -(\lambda_{io} + \lambda_{im}) \equiv -\lambda_i, \tag{3.58}$$

where λ_i indicates the total downward decay rate of the intermediate state, and

$$s_2 \approx \frac{-\Omega}{\Lambda} \approx -\left(\frac{\lambda_{mi}\lambda_{io} + \lambda_{oi}\lambda_{im}}{\lambda_{io} + \lambda_{im}}\right) = -(f_{io}\lambda_{mi} + f_{im}\lambda_{oi}). \tag{3.59}$$

From Eqs. (3.58) and (3.59), it is obvious that $|s_2| \ll |s_1|$ for s_2 involving upward transitions. Hence, the mean internal equilibration time is defined by

$$\tau_{eq} \equiv \frac{1}{|s_2|}, \tag{3.60}$$

or alternatively,

$$\begin{aligned} \frac{1}{\tau_{eq}} &\approx \frac{1}{f_{io}\lambda_{mi} + f_{im}\lambda_{oi}} \\ &= f_{im}f_{io}\lambda_i\left\{\frac{g_i}{g_m}\exp\left[-(E_i - E_m)/k_BT\right] + \frac{g_i}{g_o}\exp\left(-E_i/k_BT\right)\right\}. \end{aligned} \tag{3.61}$$

If E_m is comparable with E_i then Eq. (3.61) reduces to

$$\tau_{eq} \approx \frac{g_m}{g_i}\frac{\exp\left[(E_i - E_m)/k_BT\right]}{f_{im}f_{io}\lambda_i}. \tag{3.62}$$

Before interpreting Eq. (3.62), one has to pay special attention that: (i) the temperatures should not be too high to suppress the Boltzmann factors to unity; (ii) the two roots of $R(s)$ have to be calculated from the above Eqs. (3.55) and (3.56); (iii) The decay rates λ_{io} and λ_{im} should be adjusted by stimulated emission as discussed in Subsection 3.3.1. This simple three-level formalism has the advantage for estimating the time scale of equilibration under a given intermediate level indirectly linking the ground and isomeric states.

The general approach of examining the transitions between an isomer of a nucleus and its ground state given a number of intermediate states is not going to be discussed here. However, one can find a more general way to solve the similar types of problems in Refs. [14, 54].

3.4 Equilibration of NEEC and IC

The s-process occurs in the hot and dense plasma where ions are in highly-charged states. Once a free electron is recombined by NEEC, the electron will be soon ionised. However, the time scale of other competing ionisation processes such as collisional ionisation is expected to be shorter than one by IC—the time-reversed process of NEEC. As a result, the IC channel is closed fast and only NEEC will operate. Under these conditions,

we therefore expect that the principle of detailed balance does not hold for NEEC and IC.

To examine this point, we estimate the time scale of collisional ionisation. We take ^{152}Eu under the stellar plasma conditions as an example. The temperature is assumed to be $T_2 = 3.48 \times 10^8$ K which has been chosen in Sec. 2.2. The collisional ionisation rate is estimated from the following formula given by Ref. [55]

$$\nu_{\rm col} \approx n_e v_e 4\pi a_{\rm b}^2 \cdot \frac{U_{\rm H}^2}{U_k k_B T} \cdot \ln \frac{k_B T}{U_k}, \tag{3.63}$$

where $a_{\rm b}$ is the Bohr radius, v_e is the electron velocity and U_k and $U_{\rm H}$ are the ionisation potentials of the ionised species (here, ^{152}Eu) and hydrogen, respectively. From $\ln \frac{k_B T}{U_k}$ in the equation, it is clear that $k_B T > U_k$. For the cases where $k_B T < U_k$, $k_B T$ is approximated to U_k and $\ln \frac{k_B T}{U_k} \approx 1$. The electron density n_e is then weighted by the Maxwell-Boltzmann statistics. The time scale can be easily estimated by taking the inverse of collision rates. The results are listed in Table 3.1.

Ion configuration	Ionisation potential (keV)	$t_{\rm coll}$ (s)
H	55.780	2.079×10^{-14}
He	54.560	1.989×10^{-14}
Li	13.370	3.694×10^{-15}
Be	13.090	3.562×10^{-15}
B	12.530	3.311×10^{-15}

Table 3.1: The time scale of collisional ionisation for ^{152}Eu for different ionic configurations. The plasma is considered to be in Composition 1 at T_2.

The IC rates can be calculated from the NEEC rate by using the principle of detailed balancing. This will be shown later in Chapter 4. Again, we take ^{152}Eu as an example. The calculated time scales are listed in Table 3.2. It is obvious that the time scale of

	$t_{\rm ic}$ (s)		
Bound electron	0	1	2
$M1$	2.12×10^{-6}	2.26×10^{-6}	2.39×10^{-6}
$E2$	4.39×10^{-5}	4.66×10^{-5}	5.00×10^{-5}

Table 3.2: The time scale of IC for ^{152}Eu with different ionic configurations. The number of bound electrons is indicated. This result does not include any plasma information.

collisional ionisation is shorter than that of IC by several orders of magnitude. We can conclude that the recombined electrons in ions will be kicked out mostly by collisions and not by IC. Thus, the IC channel is closed much faster than the equilibration between

NEEC and IC can be reached. Consequently, the reaction rates for NEEC and IC can be considered separately. Using this point, we can investigate if NEEC could effectively depopulate isomers or not. To do this, we calculate the NEEC reaction rates for test isomers in the *s*-process sites. The theoretical treatment of NEEC will be discussed in detail in the next Chapter. Test isomers for the calculations will be selected in Section 5.1.

Chapter 4

Nuclear Excitation by Electron Capture

A resonant recombination process where a free electron is captured into the bound state of a highly-charged ion with the simultaneous excitation of the nucleus is called *nuclear excitation by electron capture* (NEEC). Since NEEC is a resonant process, the electronic and nuclear energy levels have to match. The recombination happens with the simultaneous excitation of the nucleus as shown in Fig. 4.1.

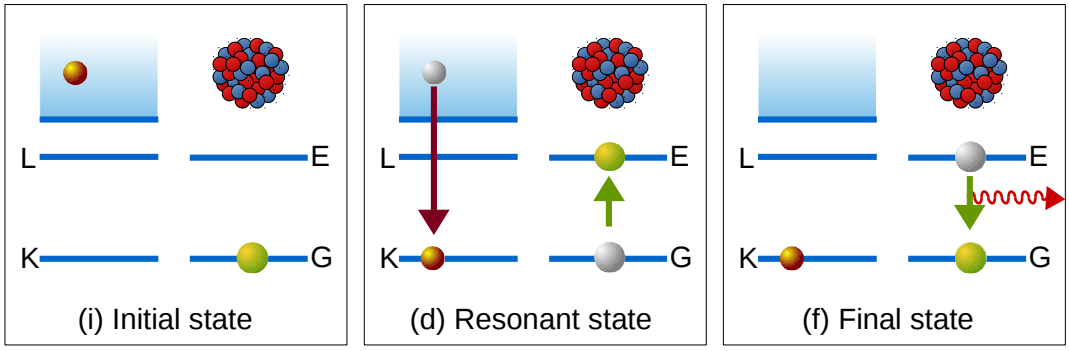

Figure 4.1: An example of NEEC recombination process. First, a free electron in the continuum is captured into the K shell of a bare nucleus (i.e., there is no bound electron). Simultaneously, the nucleus is excited from the ground state G to the excited state E. Finally, the excited nucleus decays radiatively to the ground state G (adapted from Ref. [16, 56]).

The NEEC process was first proposed theoretically by Goldanskii and Namiot in 1976 [15] and the cross section for NEEC was calculated by Yuan and Kimball [20]. Since then, NEEC has been applied to studies of recombination in plasmas [4–7] and in solid targets [17–20]. Despite the effort to demonstrate the occurrence of NEEC experimentally, a direct observation of NEEC was not yet reported. What makes the observation challenging is the extremely narrow nuclear resonances of the process. The much broader energy distribution of continuum electrons experimentally available compared to the very narrow energy range that matches with the nuclear resonance width makes it difficult to distinguish the signal from the background [56, 57]. The time-reversed process of NEEC, the internal conversion (IC) where the nuclear de-excitation occurs by kicking out a bound electron, is also a nuclear de-excitation process of interest in this work. The next Sections will be devoted to the theoretical formalism of NEEC developed by

Pálffy, including the Hamiltonian of the system, the transition amplitude and finally, the cross section. This will be performed mainly by following Chapter 1-3 of Ref. [16] and Chapter 3 of Ref. [56]. Atomic units ($m_e = \hbar = e = 1$) will be used throughout the whole calculations.

4.1 Decomposition of Fock space

The initial state $|\Psi_\mathrm{i}\rangle$ of the system is composed of the nucleus in its ground state, an electron configuration with a free electron and the radiation field in the vacuum as shown in the first diagram of Figure 4.1. The composed state vector is finally written as a direct product of nuclear, electronic and photonic states, respectively:

$$|\Psi_\mathrm{i}\rangle = |I_\mathrm{i} M_\mathrm{i}, \Psi_\mathrm{i}^\mathrm{el}, 0\rangle \equiv |I_\mathrm{i} M_\mathrm{i}\rangle \otimes |\Psi_\mathrm{i}^\mathrm{el}\rangle \otimes |0\rangle \,, \tag{4.1}$$

where the nuclear ground state is denoted by the total angular momentum I_i and its projection M_i; the electronic state is split into the bound and free electron parts—and the free electron wave function $|\mathbf{p} m_\mathrm{s}\rangle$ is denoted by its momentum $\mathbf{p}$ and spin projection quantum number m_s.
The resonant state is then reached via excitation of the nucleus by the recombination of a free electron. Meanwhile, the radiation field is still in the vacuum state as in the initial state depicted in the second diagram of Figure 4.1. The resonant state is given as

$$|\Psi_\mathrm{d}\rangle = |I_\mathrm{d} M_\mathrm{d}, \Psi_\mathrm{d}^\mathrm{el}, 0\rangle \equiv |I_\mathrm{d} M_\mathrm{d}\rangle \otimes |\Psi_\mathrm{d}^\mathrm{el}\rangle \otimes |0\rangle \,, \tag{4.2}$$

with the resonant electronic state $|\Psi_\mathrm{d}^\mathrm{el}\rangle$ given by

$$|\Psi_\mathrm{d}^\mathrm{el}\rangle = |n_\mathrm{d} \kappa_\mathrm{d} m_\mathrm{d}\rangle \,. \tag{4.3}$$

Again, the quantum numbers I_d and M_d determine the nuclear excited state; n_d, κ_d and m_d are the principal quantum number, Dirac angular momentum number, and magnetic quantum number of the bound one-electron state, respectively.
Eventually, the nuclear excited state decays radiatively back to the ground state. This final state is shown in the last diagram of the Figure 4.1. At the time, the electronic state remains unchanged. This state can be written as

$$|\Psi_\mathrm{f}\rangle = |I_\mathrm{f} M_\mathrm{f}, \Psi_\mathrm{d}^\mathrm{el}, \lambda k L M\rangle \equiv |I_\mathrm{f} M_\mathrm{f}\rangle \otimes |\Psi_\mathrm{d}^\mathrm{el}\rangle \otimes |\lambda k L M\rangle \,, \tag{4.4}$$

where the quantum numbers I_f and M_f represent the final state of the nucleus; and the de-excitation of the nucleus produces a photon which is characterised by wave number k, total angular momentum L and its projection M. The parameter λ determines that if the produced wave is of electric ($\lambda = \mathcal{E}$) or of magnetic ($\lambda = \mathcal{M}$) type. The photonic state can also be written with the photon creation operator $a^\dagger_{\lambda k L M}$ as

$$|\lambda k L M\rangle = a^\dagger_{\lambda k L M} |0\rangle \,. \tag{4.5}$$

The conjugate photon annihilation operator is $a_{\lambda k L M}$.

4.2 The Hamiltonian of the system

Since the system is concerning the interaction between the nucleus, electrons and photon, the total Hamiltonian operator of the system is naturally composed of nuclear, electronic and photonic degrees of freedom, as

$$H = H_{\mathrm{n}} + H_{\mathrm{e}} + H_{\mathrm{r}} + H_{\mathrm{en}} + H_{\mathrm{er}} + H_{\mathrm{nr}}. \tag{4.6}$$

In our framework, the nucleus is described by a *collective model*, since it is easier to relate the nuclear matrix elements with available experimental data without being affected by nuclear wave function constructions. This point is discussed in detail in Sec. 3.2 of Ref. [56]. For the case of an even-even nucleus (even number of protons and even number of neutrons), the Hamiltonian of the nucleus, H_n, can be expressed in terms of creation and annihilation operators of the collective modes, $\beta^{\dagger}_{lm}$ and β_{lm}, as

$$H_n = \sum_{lm} \omega_l \left(\beta^{\dagger}_{lm} \beta_{lm} + \frac{1}{2} \right), \tag{4.7}$$

where ω_l implies the phonon frequency.
The relativistic Dirac Hamiltonian of the free electron is written as

$$H_e = c\boldsymbol{\alpha} \cdot \mathbf{p} + (\beta - 1)c^2, \tag{4.8}$$

where $\boldsymbol{\alpha}$ is the vector composed of the Dirac matrices (α_x, α_y, α_z) and β is the fourth Dirac matrix.
The Hamiltonian of the quantised radiation field can be expressed, again, in terms of the photon creation and annihilation operators with frequency ω_k,

$$H_{\mathrm{r}} = \sum_{\lambda kLM} \omega_k a^{\dagger}_{\lambda kLM} a_{\lambda kLM}. \tag{4.9}$$

The interactions between the subspaces are expressed by remaining terms: H_{en} describing the electron-nucleus interaction, H_{er}, the electron-radiation interaction, and H_{nr}, the nucleus-radiation interaction, respectively.
For the electron-nucleus interaction, we adopt the Coulomb gauge, which allows us to separate the dominant Coulomb attraction between the electronic and the nuclear degrees of freedom,

$$H_{\mathrm{en}} = \int d^3\boldsymbol{r}_n \frac{\rho_{\mathrm{n}}(\boldsymbol{r_n})}{|\boldsymbol{r}_e - \boldsymbol{r}_n|}, \tag{4.10}$$

where $\boldsymbol{r}_e$ and $\boldsymbol{r}_n$ describe the spatial coordinates of the electron and the nucleus, respectively. The integration is performed over the entire volume of the nucleus.
The interaction of the electron and the radiation field is given by

$$H_{\mathrm{er}} = -\boldsymbol{\alpha} \cdot \boldsymbol{A} = \sum_{\lambda kLM} \left(a^{\dagger}_{\lambda kLM} \boldsymbol{\alpha} \cdot \boldsymbol{A}_{\lambda kLM}(\boldsymbol{r}) + \mathrm{H.c.} \right), \tag{4.11}$$

with the vector potential of the electromagnetic field

$$\boldsymbol{A}(\boldsymbol{r}) = \sum_{\lambda kLM} \left(\boldsymbol{A}_{\lambda kLM}(\boldsymbol{r}) a^{\dagger}_{\lambda kLM} + \boldsymbol{A}^{*}_{\lambda kLM}(\boldsymbol{r}) a_{\lambda kLM} \right). \tag{4.12}$$

The radiation field is quantised in the volume of a sphere with radius R, the two independent solutions of the wave equation for the $\boldsymbol{A}_{\lambda kLM}(\boldsymbol{r})$ are

$$\begin{aligned} \boldsymbol{A}_{(\mathcal{M})kLM}(\boldsymbol{r}) &= \sqrt{\frac{4\pi ck}{R}} j_L(kr) \boldsymbol{Y}^M_{LL}(\theta, \varphi), \\ \boldsymbol{A}_{(\mathcal{E})kLM}(\boldsymbol{r}) &= \frac{i}{k} \sqrt{\frac{4\pi ck}{R}} \nabla \times \left(j_L(kr) \boldsymbol{Y}^M_{LL}(\theta, \varphi) \right), \end{aligned} \tag{4.13}$$

where the wave number k is quantised appropriately by the boundary conditions at a perfectly conducting sphere of radius R. The term j_L represents the spherical Bessel function and $\boldsymbol{Y}^M_{LL}$ is the vector spherical harmonics, which is defined as [58]

$$\boldsymbol{Y}^M_{JL}(\theta, \varphi) = \sum_{\nu} \sum_{q} C(L\ 1\ J; \nu\ q\ M) Y_{L\nu}(\theta, \varphi) \boldsymbol{\epsilon}_q, \tag{4.14}$$

where $Y_{L\nu}$ represents the spherical harmonics [58] and the spherical vectors $\boldsymbol{\epsilon_q}$ $(q = 0, \pm 1)$ are expressed in terms of the Cartesian unit vectors as

$$\begin{aligned} \boldsymbol{\epsilon}_+ &= -\frac{1}{\sqrt{2}} (\boldsymbol{e}_x + i\boldsymbol{e}_y), \\ \boldsymbol{\epsilon}_0 &= \boldsymbol{e}_z, \\ \boldsymbol{\epsilon}_- &= \frac{1}{\sqrt{2}} (\boldsymbol{e}_x - i\boldsymbol{e}_y). \end{aligned} \tag{4.15}$$

The vector spherical harmonics are irreducible tensors of rank J with components $M = -J, \cdots, J$. Thereby, J is subject to $L - 1 \leq J \leq L + 1$.
By using the multipole expansion of the electromagnetic field, H_{nr} can be expressed in terms of the electric and magnetic multipole fields,

$$H_{\mathrm{nr}} = -\frac{1}{c} \sum_{\lambda kLM} \left(a^{\dagger}_{\lambda kLM} \int d^3\boldsymbol{r}_n \boldsymbol{j}_n(\boldsymbol{r}_n) \cdot \boldsymbol{A}_{\lambda kLM}(\boldsymbol{r}_n) + \mathrm{H.c.} \right), \tag{4.16}$$

where $\boldsymbol{j}_n$ is the nuclear current density. Again, the integration is performed over the complete nuclear volume.
The electron-nucleus interaction term H_{en} in Eq. (4.10) is responsible for the electric transitions of the nucleus. Using the collective model [59–61] with the electric multipole transition moment $\mathfrak{Q}_{lm}$ (see Appendix B of Ref. [60])

$$\mathfrak{Q}_{LM} = \int d^3r\ r^L Y_{LM}(\theta, \varphi) \rho_{\mathrm{n}}(\boldsymbol{r}), \tag{4.17}$$

where ρ_{n} represents the nuclear charge density, we can write H_{en} compactly,

$$H_{\mathrm{en}} = \sum_{LM} \frac{\mathfrak{Q}_{LM}}{R_0^l} \int d\boldsymbol{r}_n \frac{\delta(R_0 - r_n) Y_{LM}^*(\theta_n, \varphi_n)}{|\boldsymbol{r}_e - \boldsymbol{r}_n|}. \tag{4.18}$$

The full derivation is given in Ref. [16].
The Hamiltonian for the magnetic multipole transitions of the nucleus is deduced by applying the perturbation expansion to the total Hamiltonian. The first-order terms include energy corrections due to Coulomb nuclear polarisation, nuclear self-energy and electronic one-loop self energy. In the second-order term, one can identify the Hamiltonian responsible for the magnetic interaction between the electronic and nuclear currents. According to Ref. [16], the Hamiltonian for magnetic transitions reads

$$H_{\mathrm{magn}} = -\frac{1}{c} \boldsymbol{\alpha} \cdot \int d^3\boldsymbol{r}_n \frac{\boldsymbol{j}_n(\boldsymbol{r_n})}{|\boldsymbol{r}_e - \boldsymbol{r}_n|}. \tag{4.19}$$

Exploiting properties of the vector spherical harmonics for the vector potential [62] and assuming that the electron does not enter the nucleus, the interaction Hamiltonian can be expressed in terms of the magnetic multipole moment $\mathfrak{M}_{LM}$ [62]

$$H_{\mathrm{magn}} = -i \sum_{LM} \frac{4\pi}{2L+1} \sqrt{\frac{L+1}{L}} r_e^{-(L+1)} \mathfrak{M}_{LM} \boldsymbol{\alpha} \cdot \boldsymbol{Y}_{LL}^{M*}(\theta_e, \varphi_e), \tag{4.20}$$

with the magnetic multipole moment $\mathfrak{M}_{LM}$

$$\mathfrak{M}_{LM} = -\frac{i}{c} \sqrt{\frac{L}{L+1}} \int d^3r \; r^L \boldsymbol{Y}_{LL}^M(\theta, \varphi) \cdot \boldsymbol{j}_{\mathrm{n}}(\boldsymbol{r}). \tag{4.21}$$

The Hamiltonians for the electric and magnetic transitions of the nucleus in Eqs. (4.18) and (4.20) will be the basic ingredients for deriving the NEEC rates for electric and magnetic transitions in Sec. 4.4.

4.3 Total cross section for NEEC

The cross section of a given process can be expressed by the transition operator. Before we start calculating the NEEC cross section, we assume that the projection quantum numbers of $|\Psi_{\mathrm{i}}\rangle$ and $|\Psi_{\mathrm{d}}\rangle$ are not resolved in the experiment. Therefore, this part of the calculation is done by summing over the final states and averaging over the initial states. Plus, we integrate over the solid angle $\Omega_{\boldsymbol{p}}$ of the incoming electrons and average over the initial state (4π). The NEEC cross can be written as

$$\sigma_{\mathrm{neec}}^{\mathrm{i}\to\mathrm{d}} = \frac{2\pi}{F_{\mathrm{i}}} \frac{1}{2(2I_{\mathrm{i}}+1)} \sum_{M_{\mathrm{i}} m_{\mathrm{s}}} \sum_{M_{\mathrm{d}} m_{\mathrm{d}}} \frac{1}{4\pi} \int d\Omega_{\boldsymbol{p}} \frac{|\langle \Psi_{\mathrm{d}} | H_{\mathrm{magn}} + H_{\mathrm{en}} | \Psi_{\mathrm{i}} \rangle|^2 \Gamma_{\mathrm{d}} / 2\pi}{(E - E_{\mathrm{d}})^2 + \Gamma_{\mathrm{d}}^2/4}, \tag{4.22}$$

where F_{i} denotes the flux of the incoming electrons. Here, the isolated resonance approximation is applied, where only a single resonant state Ψ_{d} with resonance energy E_{d} and

natural width Γ_d is considered. The interaction Hamiltonians H_magn and H_en account for the transitions of electric and magnetic multipolarity induced by the electron-nucleus interaction which have been defined in Eqs. (4.18) and (4.20).
To write the NEEC cross section more compactly, it is convenient to introduce the NEEC rate,

$$Y_\mathrm{neec}^{\mathrm{i}\to\mathrm{d}} = \frac{2\pi}{2(2I_\mathrm{i}+1)} \sum_{M_\mathrm{i} m_\mathrm{s}} \sum_{M_\mathrm{d} m_\mathrm{d}} \int d\Omega_{\boldsymbol{p}} |\left\langle \Psi_\mathrm{d} | H_\mathrm{magn} + H_\mathrm{en} | \Psi_\mathrm{i} \right\rangle|^2 \rho_\mathrm{i}, \tag{4.23}$$

where ρ_i indicates the initial density of continuum electron states. Since the product of the incoming electron flux and ρ_i is independent of the normalisation of the continuum wave functions, we have

$$F_\mathrm{i}\rho_\mathrm{i} = \frac{p^2}{(2\pi)^3}, \tag{4.24}$$

with the absolute value p of the free electron momentum $\boldsymbol{p}$. Using Eqs. (4.23) and (4.24), the NEEC cross section becomes

$$\sigma_\mathrm{neec}^{\mathrm{i}\to\mathrm{d}} = \frac{2\pi^2}{p^2} Y_\mathrm{neec}^{\mathrm{i}\to\mathrm{d}} L_\mathrm{d}(E - E_\mathrm{d}). \tag{4.25}$$

The function L_d is the normalised Lorentz profile occurring in resonant systems,

$$L_\mathrm{d}(E - E_\mathrm{d}) = \frac{\Gamma_\mathrm{d}/2\pi}{(E-E_\mathrm{d})^2 + \Gamma_\mathrm{d}^2/4}. \tag{4.26}$$

For an arbitrary capture level $|\Psi_\mathrm{d}\rangle$, the width Γ_d can be divided into an electronic and a nuclear part,

$$\Gamma_\mathrm{d} = \Gamma_\mathrm{d}^\mathrm{el} + \Gamma_\mathrm{d}^\mathrm{nucl}. \tag{4.27}$$

The nuclear width $\Gamma_\mathrm{d}^\mathrm{nucl}$ then can be split into a radiative and an IC contribution,

$$\Gamma_\mathrm{d}^\mathrm{nucl} = \sum_{\mathrm{f}'} \left(A_\mathrm{r}^{\mathrm{d}\to\mathrm{f}'} + A_\mathrm{IC}^{\mathrm{d}\to\mathrm{f}'} \right), \tag{4.28}$$

where the superscript f' denotes the final state $|\Psi_{\mathrm{f}'}\rangle$. For the case of IC, the final state can be characterised by

$$|\Psi_{\mathrm{f}'}\rangle = |I_\mathrm{f} M_\mathrm{f}\rangle \otimes |\boldsymbol{p}' m_\mathrm{s}'\rangle \otimes |0\rangle, \tag{4.29}$$

following the notations introduced in Sec. 4.1. The IC transition rate $A_\mathrm{IC}^{\mathrm{d}\to\mathrm{f}'}$ is also related to the NEEC rate $Y_\mathrm{neec}^{\mathrm{i}\to\mathrm{d}}$ through the principle of detailed balance,

$$A_\mathrm{IC}^{\mathrm{d}\to\mathrm{f}'} = \frac{2(2I_{\mathrm{f}'}+1)}{(2I_\mathrm{d}+1)(2j_\mathrm{d}+1)} Y_\mathrm{neec}^{\mathrm{f}'\to\mathrm{d}}, \tag{4.30}$$

where j_d is the total angular momentum of the NEEC capture level which will be discussed later in Sec. 4.4. As we can see from Eq. (4.30), IC rates highly depend on the electronic structure of atoms. By adding or removing bound electrons in atomic shells, the IC rates can significantly differ. And if there is no bound electron in the atomic

shells, the IC channel is closed. For instance, a bare nucleus can only decay radiatively. In addition, it is important to note that IC happens only if the nuclear excitation energy is above the ionisation threshold of the bound electrons present, or otherwise, the de-excitation energy would not be enough to kick the bound electron into the continuum. In contrast, the radiative decay rate $A_{\mathrm{r}}^{\mathrm{d}\to\mathrm{f}}$ is independent of the electronic structure. It is determined by the nuclear matrix element of H_{nr}. In the case of radiative decay, the final state will correspond to Eq. (4.4). The radiative decay rate then can be written as

$$A_{\mathrm{r}}^{\mathrm{d}\to\mathrm{f}'} = \frac{2\pi}{2I_{\mathrm{d}}+1} \sum_{M_{\mathrm{f}'}M} \sum_{M_{\mathrm{d}}} |\langle \Psi_{\mathrm{f}'}|H_{\mathrm{nr}}|\Psi_{\mathrm{d}}\rangle|^2 \rho_{\mathrm{f}}. \tag{4.31}$$

The matrix elements of H_{nr} are connected to the reduced transition probabilities $\mathcal{B}$, for a given multipolarity L,

$$A_{\mathrm{r}}^{\mathrm{d}\to\mathrm{f}'}(\lambda, L) = \frac{8\pi(L+1)}{L[(2L+1)!!]^2} \left(\frac{E_{\mathrm{n}}}{c}\right)^{2L+1} \mathcal{B}(\lambda L, I_{\mathrm{d}} \to I_{\mathrm{f}'}), \tag{4.32}$$

where λ determines again if the type of transition is electric ($\lambda = \mathcal{E}$) or magnetic ($\lambda = \mathcal{M}$) and E_{n} is the energy of the excited nuclear state. According to the principle of detailed balance, the reduced transition probabilities for absorbing a photon is related through the formula

$$\mathcal{B}(\lambda L, I_{\mathrm{d}} \to I_{\mathrm{f}'}) = \frac{2I_{\mathrm{f}'}+1}{2I_{\mathrm{d}}+1} \mathcal{B}(\lambda L, I_{\mathrm{f}'} \to I_{\mathrm{d}}). \tag{4.33}$$

Often, it is more reasonable to use the integrated cross section instead of $\sigma_{\mathrm{neec}}^{\mathrm{i}\to\mathrm{d}}$, since the peak value on resonance $E = E_{\mathrm{d}}$ can be very large, while the width of the resonance is very narrow. Integrating Eq. (4.25) over the continuum energy E and assuming that p^2 and $Y_{\mathrm{neec}}^{\mathrm{i}\to\mathrm{d}}$ are constant over the very narrow region Γ_d, the resonance strength $S_{\mathrm{neec}}^{\mathrm{i}\to\mathrm{d}}$ is given as

$$S_{\mathrm{neec}}^{\mathrm{i}\to\mathrm{d}} = \frac{2\pi^2}{p^2} Y_{\mathrm{neec}}^{\mathrm{i}\to\mathrm{d}}. \tag{4.34}$$

Up to now, the population of the nuclear excited state via NEEC is discussed. In the second step, the nuclear decay has to be considered with branching ratio. The two-step resonance strength for NEEC followed by the nuclear decay is expressed as

$$S_{\mathrm{neec}}^{\mathrm{i}\to\mathrm{f}} = \frac{2\pi^2}{p^2} Y_{\mathrm{neec}}^{\mathrm{i}\to\mathrm{d}} B^{\mathrm{d}\to\mathrm{f}}. \tag{4.35}$$

The branching ratio $B^{\mathrm{d}\to\mathrm{f}}$ describes the probability of the nuclear state d decaying into considered decay channel f. For example, if the NEEC decays via IC, the branching ratio evaluates to

$$B_{\mathrm{IC}}^{\mathrm{d}\to\mathrm{f}} = \frac{A_{\mathrm{IC}}^{\mathrm{d}\to\mathrm{f}}}{\Gamma_{\mathrm{d}}^{\mathrm{nucl}}}. \tag{4.36}$$

4.4 Excitation rates via NEEC

To calculate the NEEC rate $Y_{\rm neec}^{\rm i\to d}$, we have to calculate the matrix elements of transitions. In this Section, we will focus on calculating the electronic matrix elements and connecting the nuclear matrix elements with the reduced nuclear transition probabilities.

4.4.1 Electric transitions

For electric transitions, the rate is related to the matrix element of the Coulomb interaction Hamiltonian $H_{\rm en}$ in Eq. (4.18). Taking the electric interaction part from Eq. (4.23) and inserting Eq. (4.18), we have

$$\begin{aligned} Y_{\rm neec}^{\mathcal{E}} &= \frac{2\pi}{2(2I_{\rm i}+1)}\sum_{M_{\rm i}m_{\rm s}}\sum_{M_{\rm d}m_{\rm d}}\int d\Omega_{\boldsymbol{p}}|\left\langle\Psi_{\rm d}|H_{\rm en}|\Psi_{\rm i}\right\rangle|^2\rho_{\rm i} \\ &= \frac{2\pi}{2(2I_{\rm i}+1)}\sum_{M_{\rm i}m_{\rm s}}\sum_{M_{\rm d}m_{\rm d}}\int d\Omega_{\boldsymbol{p}} \\ &\times|\left\langle I_{\rm d}M_{\rm d},n_{\rm d}\kappa_{\rm d}m_{\rm d},0|\sum_{lm}\frac{\mathfrak{Q}_{lm}}{R_0^l}\int d\boldsymbol{r}_n\frac{\delta(R_0-r_n)Y_{lm}^*(\theta_n,\varphi_n)}{|\boldsymbol{r}_e-\boldsymbol{r}_n|}|I_{\rm i}M_{\rm i},\boldsymbol{p}m_{\rm s},0\right\rangle|^2\rho_{\rm i}. \end{aligned} \tag{4.37}$$

Applying the multipole expansion

$$\frac{1}{|\boldsymbol{r}_e-\boldsymbol{r}_n|}=\sum_{L=0}^{\infty}\sum_{M=-L}^{L}\frac{4\pi}{2L+1}Y_{LM}(\theta_{\rm n},\varphi_{\rm n})Y_{LM}^*(\theta_{\rm e},\varphi_{\rm e})\frac{r_<^L}{r_>^{L+1}}, \tag{4.38}$$

the electric interaction Hamiltonian becomes

$$H_{\rm en}=\sum_{LM}\frac{4\pi}{2L+1}\frac{\mathfrak{Q}_{LM}}{R_0^L}Y_{LM}^*(\theta_{\rm e},\varphi_{\rm e})\int_0^{\infty}dr_nr_n^2\frac{r_<^L}{r_>^{L+1}}\delta(R_0-r_n). \tag{4.39}$$

The notations $r_<$ and $r_>$ stand for the smaller and the larger values of two radii r_e and r_n, respectively. The matrix element of the Hamiltonian reads

$$\begin{aligned} (H_{\rm en})_{\rm di} &= \frac{1}{R_0^L}\sum_{LM}\frac{4\pi}{2L+1}\left\langle I_{\rm d}M_{\rm d}|\mathfrak{Q}_{LM}|I_{\rm i}M_{\rm i}\right\rangle \\ &\times\left\langle n_{\rm d}\kappa_{\rm d}m_{\rm d}|Y_{LM}^*(\theta_{\rm e},\varphi_{\rm e})\int_0^{\infty}dr_nr_n^2\frac{r_<^L}{r_>^{L+1}}\delta(R_0-r_n)|\boldsymbol{p}m_{\rm s}\right\rangle. \end{aligned} \tag{4.40}$$

As we can see from Eq. (4.40), the matrix element of the electron-nucleus interaction Hamiltonian is composed of electronic and nuclear parts. The nuclear part can be written in terms of the reduced element of the electric multipole operator $\mathfrak{Q}_{LM}$, as in Ref. [58],

$$\left\langle I_{\rm d}M_{\rm d}|\mathfrak{Q}_{LM}|I_{\rm i}M_{\rm i}\right\rangle=\frac{(-1)^{I_{\rm i}-M_{\rm i}}}{\sqrt{2L+1}}C(I_{\rm d}\ I_{\rm i}\ L;M_{\rm d}\ \text{-}M_{\rm i}\ M)\left\langle I_{\rm d}\|\mathfrak{Q}_{LM}\|I_{\rm i}\right\rangle. \tag{4.41}$$

Here, $C(I_\mathrm{d}\ I_\mathrm{i}\ L; M_\mathrm{d}\ \text{-}M_\mathrm{i}\ M)$ stands for the Clebsch-Gordan coefficient. The squared modulus of the reduced nuclear matrix element is proportional to the reduced transition probability of a certain multipolarity L,

$$\mathcal{B}(\mathcal{E}L, I_\mathrm{i} \to I_\mathrm{d}) = \frac{1}{2I_\mathrm{i}+1} |\langle I_\mathrm{d} \| \mathfrak{Q}_L \| I_\mathrm{i} \rangle|^2, \tag{4.42}$$

whose values are available from experimental databases.
To evaluate the electronic matrix element, we expand the initial continuum electronic wave function in partial waves as in Ref. [63],

$$|\boldsymbol{p} m_\mathrm{s}\rangle = \sum_{\kappa m} i^l e^{i\Delta_\kappa} \sum_{m_l} Y^*_{lm_l}(\theta_{\boldsymbol{p}}, \varphi_{\boldsymbol{p}}) C\left(l\ \frac{1}{2}\ j; m_l\ m_s\ m\right) |\epsilon\kappa m\rangle\,, \tag{4.43}$$

where ϵ is the energy of the continuum electron measured from the ionisation threshold, $\epsilon = \sqrt{p^2c^2 + c^4} - c^2$, κ is the eigenvalue of the relativistic spin-orbit operator. The total and orbital angular momentum of the partial wave are defined as j and l. Δ_κ is the Coulomb phase which ensures the correct boundary conditions. With these specifications, we can write the NEEC rate for a given electric multipolarity L as

$$Y^{\mathcal{E}}_\mathrm{neec} = \frac{4\pi^2\rho_i}{(2L+1)^2} R_0^{-2(L+2)} \mathcal{B}(\mathcal{E}L, I_\mathrm{i} \to I_\mathrm{d})(2j_\mathrm{d}+1) \sum_\kappa |R^{\mathcal{E}}_{L,\kappa_\mathrm{d},\kappa}|^2 C\left(j_\mathrm{d}\ L\ j; \frac{1}{2}\ 0\ \frac{1}{2}\right)^2, \tag{4.44}$$

with the electronic radial integral

$$\begin{aligned} R^{\mathcal{E}}_{L,\kappa_\mathrm{d},\kappa} = {} & \frac{1}{R_0^{L-1}} \int_0^{R_0} dr_\mathrm{e} r_\mathrm{e}^{L+2} \Big[f_{n_\mathrm{d}\kappa_\mathrm{d}}(r_\mathrm{e}) f_{\epsilon\kappa}(r_\mathrm{e}) + g_{n_\mathrm{d}\kappa_\mathrm{d}}(r_\mathrm{e}) g_{\epsilon\kappa}(r_\mathrm{e}) \Big] \\ & + R_0^{L+2} \int_{R_0}^{\infty} dr_\mathrm{e} r_\mathrm{e}^{-L+1} \Big[f_{n_\mathrm{d}\kappa_\mathrm{d}}(r_\mathrm{e}) f_{\epsilon\kappa}(r_\mathrm{e}) + g_{n_\mathrm{d}\kappa_\mathrm{d}}(r_\mathrm{e}) g_{\epsilon\kappa}(r_\mathrm{e}) \Big]. \end{aligned} \tag{4.45}$$

In the electronic radial integrals, $f_{\epsilon\kappa}$ and $g_{\epsilon\kappa}$ are the small and large radial components of the relativistic continuum electron wave function

$$\Psi_{\epsilon\kappa m}(\boldsymbol{r}) = \begin{pmatrix} g_{\epsilon\kappa}(r)\Omega^m_\kappa(\theta,\varphi) \\ i f_{\epsilon\kappa}(r)\Omega^m_{-\kappa}(\theta,\varphi) \end{pmatrix}, \tag{4.46}$$

and $f_{n_\mathrm{d}\kappa_\mathrm{d}}$ and $g_{n_\mathrm{d}\kappa_\mathrm{d}}$ are the components of the bound Dirac wave functions

$$\Psi_{n_\mathrm{d}\kappa_\mathrm{d}}(\boldsymbol{r}) = \begin{pmatrix} g_{n_\mathrm{d}\kappa_\mathrm{d}}(r)\Omega^{m_\mathrm{d}}_{\kappa_\mathrm{d}}(\theta,\varphi) \\ i f_{n_\mathrm{d}\kappa_\mathrm{d}}(r)\Omega^{m_\mathrm{d}}_{-\kappa_\mathrm{d}}(\theta,\varphi) \end{pmatrix}, \tag{4.47}$$

with the spin-angular functions Ω^m_κ. The radial integral $R^{\mathcal{E}}_{L,\kappa_\mathrm{d},\kappa}$ is calculated numerically.

4.4.2 Magnetic transitions

Similarly, using the Hamiltonian $H_{\rm magn}$ in Eq. (4.20), the matrix element of the NEEC rate for magnetic transitions can be written as

$$\begin{aligned}(H_{\rm en})_{\rm di} = 4\pi i \sum_{LM} (-1)^M \sqrt{\frac{L+1}{L}} \frac{1}{2L+1} \langle I_{\rm d} M_{\rm d} | \mathfrak{M}_{LM} | I_{\rm i} M_{\rm i} \rangle \\ \times \langle n_{\rm d} \kappa_{\rm d} m_{\rm d} | r_e^{-(L+1)} \boldsymbol{\alpha} \cdot \boldsymbol{Y}_{LL}^{-M}(\theta_e, \varphi_e) | \boldsymbol{p} m_{\rm s} \rangle \,,\end{aligned} \tag{4.48}$$

where the complex conjugate of the vector spherical harmonics is used [64],

$$\boldsymbol{Y}_{JL}^{M*} = (-1)^{L+J+M+1} \boldsymbol{Y}_{JL}^{-M}. \tag{4.49}$$

Again, the nuclear matrix element can be expressed in terms of the reduced magnetic transition probability of a certain multipolarity L,

$$\mathcal{B}(\mathcal{M}L, I_{\rm i} \to I_{\rm d}) = \frac{1}{2I_{\rm i}+1} |\, \langle I_{\rm d} \| \mathfrak{M}_L \| I_{\rm i} \rangle \,|^2. \tag{4.50}$$

The electronic matrix element

$$\langle n_{\rm d} \kappa_{\rm d} m_{\rm d} | r_e^{-(L+1)} \boldsymbol{\alpha} \cdot \boldsymbol{Y}_{LL}^{-M}(\theta_e, \varphi_e) | \boldsymbol{p} m_{\rm s} \rangle \tag{4.51}$$

can be evaluated by expanding the initial continuum wave function $|\boldsymbol{p} m_{\rm s}\rangle$ with proper quantum numbers κ, m, as in Eq. (4.43). First, one inserts the vector spherical harmonics in Eq. (4.14) into Eq. (4.51) and then performs the analytical angular integration. Or alternatively, one can use the properties of spherical tensors to do the same calculation more compactly. This calculation is shown in Appendix C of Ref. [16]. After the calculations, the electronic matrix elements can be written as

$$\begin{aligned}&\langle n_{\rm d} \kappa_{\rm d} m_{\rm d} | r_e^{-(L+1)} \boldsymbol{\alpha} \cdot \boldsymbol{Y}_{LL}^{-M}(\theta_e, \varphi_e) | \boldsymbol{p} m_{\rm s} \rangle \\ &= i(-1)^{j-L+\frac{1}{2}} \sqrt{\frac{(2j+1)(2L+1)}{4\pi L(L+1)}} C(j\ L\ j_{\rm d}; m\ {-M}\ m_{\rm d}) \begin{pmatrix} j_{\rm d} & j & L \\ \frac{1}{2} & -\frac{1}{2} & 0 \end{pmatrix} \\ &\times (\kappa_{\rm d} + \kappa) \int_0^\infty dr_{\rm e} r_{\rm e}^{-L+1} \Big[g_{n_{\rm d}\kappa_{\rm d}}(r_{\rm e}) f_{\epsilon\kappa}(r_{\rm e}) + f_{n_{\rm d}\kappa_{\rm d}}(r_{\rm e}) g_{\epsilon\kappa}(r_{\rm e}) \Big],\end{aligned} \tag{4.52}$$

where the relation between the Wigner $3j$-symbol and the Clebsch-Gordan coefficient is given by

$$C(j_1\ j_2\ j; m_1\ m_2\ m) = (-1)^{m+j_1-j_2} \sqrt{2j+1} \begin{pmatrix} j_1 & j_2 & j \\ m_1 & m_2 & -m \end{pmatrix}. \tag{4.53}$$

Combining the above equations, the NEEC rate for magnetic transitions with a fixed multipolarity L is obtained

$$\begin{aligned}Y_{\rm neec}^{\mathcal{M}} = \frac{4\pi^2 \rho_{\rm i}}{L^2(2L+1)^2} \mathcal{B}(\mathcal{M}L, I_{\rm i} \to I_{\rm d})(2j_{\rm d}+1) \\ \times \sum_{\kappa} (2j+1)(\kappa_{\rm d}+\kappa) \begin{pmatrix} j_{\rm d} & j & L \\ \frac{1}{2} & -\frac{1}{2} & 0 \end{pmatrix}^2 |R_{L,\kappa_{\rm d},\kappa}^{\mathcal{M}}|^2,\end{aligned} \tag{4.54}$$

where the magnetic radial integral $R^{\mathcal{M}}_{L,\kappa_\mathrm{d},\kappa}$ is defined as

$$R^{\mathcal{M}}_{L,\kappa_\mathrm{d},\kappa} = \int_0^\infty dr_\mathrm{e} r_\mathrm{e}^{-L+1}\Big[g_{n_\mathrm{d}\kappa_\mathrm{d}}(r_\mathrm{e})f_{\epsilon\kappa}(r_\mathrm{e}) + f_{n_\mathrm{d}\kappa_\mathrm{d}}(r_\mathrm{e})g_{\epsilon\kappa}(r_\mathrm{e})\Big]. \tag{4.55}$$

Analogously, the magnetic radial integral is solved with a numerical approach as $R^{\mathcal{E}}_{L,\kappa_\mathrm{d},\kappa}$.

4.5 NEEC reaction rates in a plasma

The NEEC is a resonant process which has a very narrow resonance bandwidth. However, free electrons are distributed with a relatively wide range of kinetic energies in a plasma. This means that over the broad kinetic energy distribution of the free electrons, many resonant NEEC channels can exist. In this Section, following Sec. 4.1 of Ref. [56], we will describe the theoretical formalism for calculating the NEEC reaction rate when many NEEC channels are possible.
As introduced in Sec. 4.1, the initial and the intermediate states follow the notations in Eqs. (4.1) and (4.2), respectively. To restrict the number of possible initial configurations, we assume that the free electrons recombine only to the ions in their ground states. Thereby, the initial electronic configuration α_0 is uniquely defined by the the charge state number q before the electron capture. Using the isolated resonance approximation, the total NEEC reaction rate in a plasma can be expressed as a summation over all possible charge states q and all capture channels α_d,

$$\lambda_\mathrm{neec} = \sum_q \sum_{\alpha_\mathrm{d}} P_q \lambda^{q,\alpha_\mathrm{d}}_\mathrm{neec}, \tag{4.56}$$

where the factor P_q denotes the probability of an ion in the charge state q in the plasma, and the partial NEEC rate into the capture level α_d of an ion in the charge state q is given by

$$\lambda^{q,\alpha_\mathrm{d}}_\mathrm{neec} = \int dE\ \sigma^{\mathrm{i}\to\mathrm{d}}_\mathrm{neec}\phi_\mathrm{e}(E). \tag{4.57}$$

The single-resonance cross section $\sigma^{\mathrm{i}\to\mathrm{d}}_\mathrm{neec}$ is given by Eq. (4.25). The dependence on the charge state q enters $\sigma^{\mathrm{i}\to\mathrm{d}}_\mathrm{neec}$ in the Lorentz profile. The electron flux ϕ_e in the plasma can be written as the product of the density of states $g(E)$, the Fermi-Dirac distribution $f_\mathrm{FD}(E, T_\mathrm{e})$ for a certain electron temperature T_e and the velocity $v(E)$,

$$\phi_\mathrm{e}(E) = g(E)f_\mathrm{FD}(E, T_\mathrm{e})v(E). \tag{4.58}$$

The electron flux ϕ_e depends on the temperature T_e and this dependence is included in the Fermi-Dirac distribution f_FD. The density of states $g(E)$ and the velocity $v(E)$ are determined by the relativistic dispersion relation of the free electrons. The chemical potential of the electrons which appears in f_FD is determined via the normalisation

$$\int dE\ g(E)f_\mathrm{FD}(E, T_\mathrm{e}) = n_\mathrm{e}, \tag{4.59}$$

where n_e represents the number density of the free electrons. Using the definition of the NEEC cross section and the assumption that the momentum of the free electron and the NEEC interaction matrix elements are constant over the resonance width of the Lorentz profile $L_d(E - E_d)$, Eq. (4.57) becomes

$$\lambda_{\text{neec}}^{q,\alpha_d} = \frac{2\pi^2}{p^2} Y_{\text{neec}}^{i\to d} \Phi_e^{\text{res}}(E_d), \tag{4.60}$$

where the resonant electron flux is given by

$$\Phi_e^{\text{res}}(E_d) = \int dE\ L_d(E - E_d)\phi_e(E). \tag{4.61}$$

Since the resonance width of NEEC is narrow in comparison to the energy scale on which ϕ_e is varying, in this work, the Lorentz profile is approximated by a delta function. With this assumption, we can write the resonant electron flux as

$$\Phi_e^{\text{res}}(E_d) \approx \int_0^\infty dE\ \delta(E - E_d)\phi_e(E) = \phi_e(E_d). \tag{4.62}$$

Hence, the partial NEEC rate in a plasma is given by

$$\lambda_{\text{neec}}^{q,\alpha_d} = \frac{2\pi^2}{p^2} Y_{\text{neec}}^{i\to d} \phi_e(E_d). \tag{4.63}$$

The total NEEC reaction rate λ_{neec} in Eq. (4.56) highly depends on the charge states q and the free electron energies which are extracted from the plasma conditions. The momenta and the energies of the free electrons will be determined by the relativistic dispersion relation as mentioned above with the according resonant channels, and P_q, the probability of an ion in charge state q, will be calculated by the Saha ionisation equation introduced in Sec. 3.2.

Chapter 5

Numerical Results

Our goal is to investigate if NEEC can efficiently populate or depopulate isomers in the neutron capture synthesis. To this end, we want to calculate the net NEEC rates in the stellar plasma. Before the calculation, first, the physical site of the *s*-process has to be identified to determine the conditions of our stellar plasmas. The relevant physical parameters are determined in Sec. 2.2. The chosen temperatures and plasma compositions are summarised in Table 5.1. The mass density of plasmas is chosen as $\rho = 10$ g/cm^{-3} from Table. 2.1. The test isomers are selected as well in Sec. 5.1. Using Eqs. (4.56) and (4.63), the total NEEC reaction rate can be written as

$$\lambda_{\mathrm{neec}} = \sum_{q} P_q \sum_{\alpha_{\mathrm{d}}} \frac{2\pi^2}{p^2} Y_{\mathrm{neec}}^{\mathrm{i}\to\mathrm{f}} \Phi_e^{\mathrm{res}}. \tag{5.1}$$

The calculation of λ_{neec} in plasmas can be divided into four parts:

I solving the Saha equation to obtain the probability P_q of an ion to be in the charge state q in the plasma;

II calculating the NEEC rates $Y_{\mathrm{neec}}^{\mathrm{i}\to\mathrm{d}}$ for specific nuclear transitions involving an isomer;

III evaluating the electron flux Φ_e^{res} by integrating the Fermi-Dirac distribution.

Parts I and II will be presented in Sec. 5.2 and 5.3, respectively. Part III will be calculated by using Eq. (4.58) as

$$\phi_{\mathrm{e}}(E) = g(E) f_{\mathrm{FD}}(E, T) v(E). \tag{5.2}$$

Finally, plugging the results of I, II and III into Eq. (5.1), we obtain λ_{neec}. The calculated resonant electron flux will be presented with the total NEEC reaction rates in Sec. 5.4.

Elements	H	He	C	O	Temperatures (K)	
Composition 1	-	78%	20%	2%	T_1	0.9×10^8
Composition 2	75%	25%	-	-	T_2	3.48×10^8

Table 5.1: Chosen plasma compositions and temperatures for the *s*-process physical sites. The percentages are given in terms of mass fractions.

5.1 Selection of isomers

Our focus is on those elements in which the nuclear energy level populations are not expected to follow the Maxwell-Boltzmann distribution. To examine the impact of NEEC in the s-process nucleosynthesis, we first chose 19 isomers from Refs. [9, 12, 65]. These isomeric levels are not expected to be equilibrated with the respective ground states due to their different beta decay rates and to a strong population via gamma decay cascades following neutron capture. The relevant nuclear data is presented in Table 5.2. Among those candidates, five isomers are finally selected for actual calculations. The criteria used for the selection are as follows:

i the low-lying energy levels are of order k_BT, i.e., thermal energy;

ii nuclear transition probabilities are available from experimental databases;

iii the IC coefficients in given transitions are large so that IC is significant;

iv isomers possibly beta decay.

The selected isomers are: ^{58m}Co, ^{99m}Tc, ^{121m}Sn, ^{124m}Sb, and ^{152m}Eu. Their nuclear levels are shown in Fig. 5.1. Some of their features are discussed in more detail in the following:

^{58m}Co: Coulomb enhancement (stellar enhancement of the radiative transition rates of nuclear excited states by Coulomb interactions among charged particles) ratios of isomeric transitions in explosive nucleosynthesis are calculated for ^{58m}Co and other isomers in Ref. [9]. The Coulomb enhancement may link isomers to higher-lying excited states and these links can be significant in determining the rate at which these isomers are brought into thermal equilibrium with their ground states under stellar conditions.

^{99m}Tc: Technetium (Tc) has three long-lived isotopes of atomic numbers A =97, 98 and 99, respectively. The isotope ^{98}Tc is shielded with respect to both β^+- and β^--decays by stable isobars of ruthenium (Ru) and molybdenum (Mo). The isotope ^{97}Tc is only produced by the p-process (fast proton capture process) whose detailed mechanism and site are not clear. Pure p-process isotopes are very rare, though A =97 is close to ^{92}Mo and ^{94}Mo, which are among the most frequent p-process-only nuclides in the solar system. Based on these facts, it is generally assumed that the Tc isotope present in stars is ^{99}Tc which can be produced in both s- and r-process. However, these stars do not have the high neutron densities required for the r-process and the He burning shells in red-giants are the most probable sites for the s-process. Therefore, Tc is produced by a pure s-process [66].

^{121}Sn with ^{123}Sn and ^{124}Sn might be important for studying s-only nuclei $^{122-124}$Te. β-lifetimes of the isomer and the ground state are shorter than the n-capture time scale [12]. Also ^{121m}Sn is interesting for the fact that its lifetime is much longer than that of the ground state, and it is possible for a certain fraction of the ground state ^{121}Sn to be exhausted in the s-process as a result of neutron capture by the isomeric state. These instances can be used to estimate the s-process time scale and further, one can separate the r-process contribution from the synthesis of ^{121}Sn [65].

^{124m}Sb: If ^{124m}Sb is not equilibrated due to enhanced beta decay rate under the stellar conditions, the β-half-life of the isomer would be close to the value for the ground state ($\sim$ 60 days). Because the isomer is not significantly fed by n-capture and the excitation from the ground state takes a long time [12].

^{152m}Eu: Analysing the path of neutron captures in region A=150-156 enables us to find the s-process contributions to the abundances of the nuclides ^{152}Gd and ^{154}Gd as a function of the neutron flux. The lower bound of neutron flux is determined by the abundance of ^{152}Gd which depends on the isomer ratio of ^{152}Eu. The determination of the value of neutron flux is hindered by the lack of information on the contribution made by the p-process to the synthesis of ^{154}Gd and ^{152}Gd [65].

Isomer	Energy (keV)	Lifetime	Transition type	IC coefficient	Reference
^{34m}Cl	146.36	31.99 min	M3	0.1656	[9]
^{46m}Sc	142.528	18.75 s	E3	0.612	[9]
^{58m}Co	24.95	9.10 h	M3	2.52×10^3	[9]
^{79m}Se	95.77	3.92 min	E3	9.48	[12, 65]
^{85m}Kr	304.871	4.480 h	M4	0.511	[9, 12, 65]
^{99m}Tc	140.5106	0.19 ns	M1+E2	0.113	[12]
^{113m}Cd	263.54	14.1 y	E5	4.24	[9, 12, 65]
^{114m}In	190.2682	49.51 d	E4	5.04	[9]
^{115m}In	336.244	4.486 h	M4	1.081	[9, 12]
^{115m}Cd	181.0	44.56 d	M1+E2	$\approx$0.0749	[12]
^{121m}Sn	6.31	43.9 y	M4	8.7×10^{10}	[12, 65]
^{123m}Sn	24.6	40.06 min	-	-	[9, 12]
^{124m}Sb	36.8440	20.2 min	E3	2.97×10^4	[12]
^{134m}Cs	11.2442	46.6 ns	-	-	[12]
^{148m}Pm	137.9	41.29 d	E4	1.23×10^4	[9, 12]
^{152m}Eu	45.5998	9.3116 h	-	-	[9, 12, 65]
^{166m}Ho	5.969	$1.20 \cdot 10^3$y	-	-	[9, 65]
^{176m}Lu	122.845	3.664 h	-	-	[9, 65]
^{180m}Ta	77.2	$> 7.1 \cdot 10^{15}$y	-	-	[9, 12]

Table 5.2: Considered isomer candidates. IC coefficients are given for the transitions from the isomeric states to the ground states (data is taken from Nuclear Structure and Decay Databases [67]).

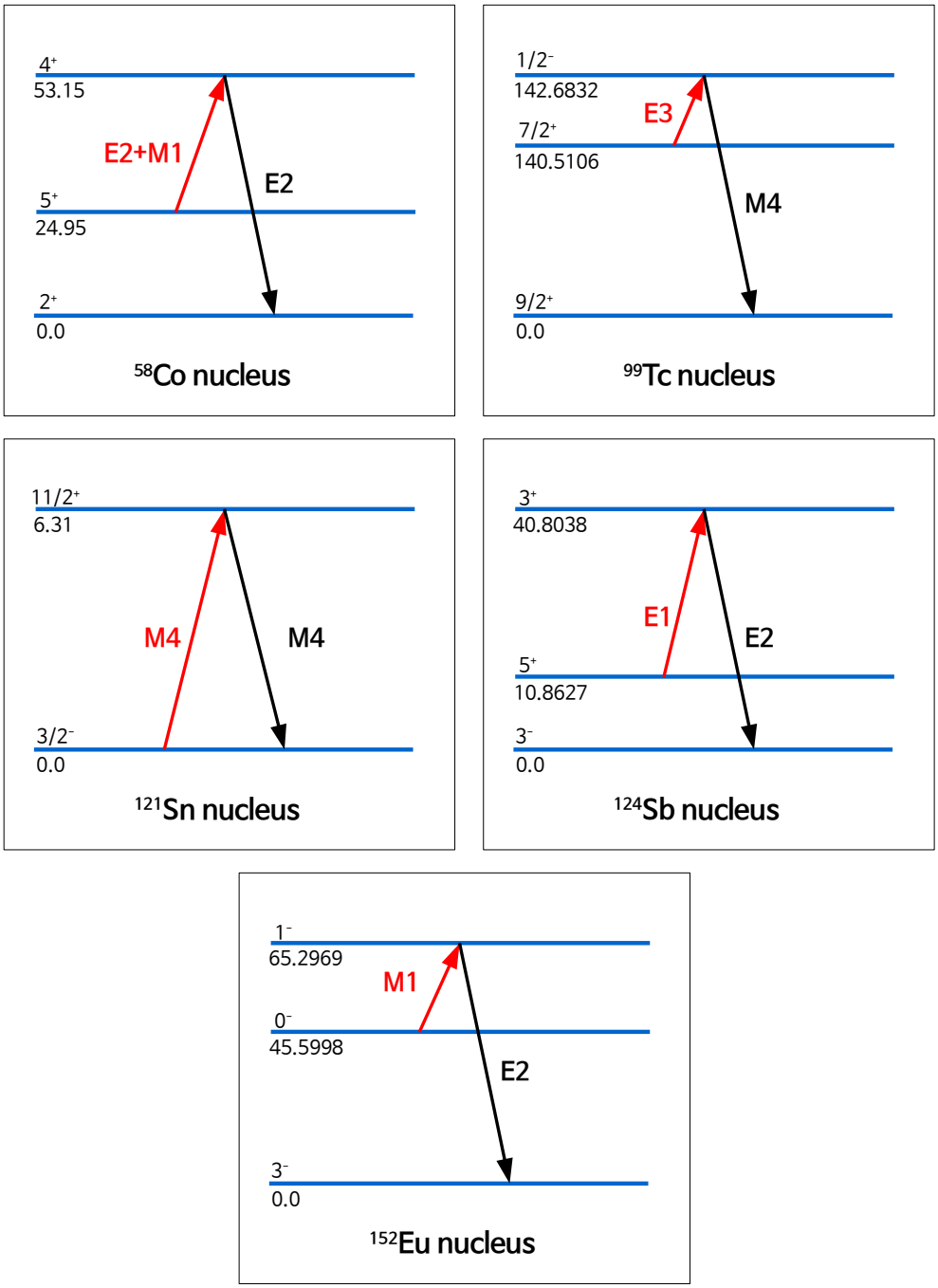

Figure 5.1: Nuclear excitation by electron capture for isomer triggering in ^{58m}Co, ^{99m}Tc, ^{124m}Sb, ^{152m}Eu and ground state excitation in ^{121m}Sn. The nuclear levels are labeled with their total angular momentum, parity, and energy (in keV).

5.2 Charge states of ions in the plasma

5.2.1 Chemical potential

The degree of ionisation in the considered stellar plasmas is evaluated with the help of the Saha ionisation equation given in Eq. (3.22)

$$\frac{n_{i,j+1}}{n_{i,j}} = \frac{b_{i,j+1}}{b_{i,j}} \cdot \left(\frac{m_{i,j+1}}{m_{i,j}}\right)^{3/2} \cdot \exp\left(\frac{m_e c^2}{k_B T} - \frac{I_{i,j}}{k_B T} - \frac{\mu_e}{k_B T}\right). \tag{5.3}$$

The unknown chemical potential μ_e can be evaluated by using the relation between μ_e and electron energy, and the charge neutrality of plasmas. The degeneracy parameter included in Eq. (3.22) can be defined as

$$\eta = \frac{\mu_e - m_e c^2}{k_B T}. \tag{5.4}$$

As a result, the electron number density (3.13) needed for calculating μ_e will be changed. As the relativistic energy of electrons is given by $E_e = \sqrt{m_e^2 c^4 + p^2 c^2}$, we define new variables

$$\omega := \sqrt{1 + \frac{p^2}{m_e^2 c^2}} \quad \text{and} \quad \beta := \frac{m_e c^2}{k_B T}. \tag{5.5}$$

Hence, we obtain

$$\frac{E_e}{k_B T} = \beta\omega, \;\; p = m_e c\sqrt{\omega^2 - 1} \;\; \text{and} \;\; \frac{dp}{d\omega} = \frac{m_e c\omega}{\sqrt{\omega^2 - 1}}. \tag{5.6}$$

Then n_e in Eq. (3.13) becomes

$$n_e = \frac{8\pi m_e^3 c^3}{h^3} \int_1^\infty \frac{\omega\sqrt{\omega^2 - 1}}{\exp\left(\beta\omega - \mu_e/k_B T\right)} d\omega = \frac{8\pi m_e^3 c^3}{h^3} \int_1^\infty \frac{\omega\sqrt{\omega^2 - 1}}{\exp\left[\beta(\omega - 1) - \eta\right]} d\omega. \tag{5.7}$$

Using the charge neutrality, we can get another expression for n_e. The charge neutrality assumes that electrons released from atoms by ionisation processes will contribute to n_e in the plasma. Given total number density ρ and the individual mass fraction x_i of atomic species i, we can calculate the atom number densities $n_{i,j}$ if the masses $m_{i,j}$ are known with the ionisation states j:

$$\sum_j m_{i,j} n_{i,j} = \rho x_i. \tag{5.8}$$

Using Eq. (5.8), we can assign the charge numbers j to the ion densities and calculate n_e from

$$n_e = \rho \sum_i x_i \left(\frac{\sum_j j n_{i,j}}{\sum_j m_{i,j} n_{i,j}}\right) = \sum_{i,j} j n_{i,j}. \tag{5.9}$$

The ion masses can be approximated by the neutral masses (as will be discussed in the following Section). The electron density n_e will be calculated by Eq. (5.9). Then the obtained n_e is plugged into Eq. (5.7) to evaluate the degeneracy parameter η.

5.2.2 Approximations

The Saha ionisation equation has been introduced in Sec. 3.2. Before the actual calculations, the equation can be simplified with some approximations. Since the mass of nucleons is much higher than that of electrons, the ion masses can be approximated by the atomic masses. Thus, we obtain from Eq. (3.22),

$$\frac{n_{i,j+1}}{n_{i,j}} \approx \frac{b_{i,j+1}}{b_{i,j}} \cdot \exp\left(\frac{m_e c^2}{k_B T} - \frac{I_{i,j}}{k_B T} - \frac{\mu_e}{k_B T}\right). \tag{5.10}$$

In addition, the ion number densities in Eq. (5.8) can be calculated from

$$\sum_j n_{i,j} \approx \frac{\rho x_i}{m_i}. \tag{5.11}$$

The ionisation distribution for the sum in Eq. (5.11) is calculated by a self-consistent method. We assume that composition elements (H, He, C, O) in the plasma are fully ionised for the considered temperatures ($k_B T_1 \approx 7.76$ keV and $k_B T_2 \approx 30$ keV). This assumption is reasonable, since the uncorrected ionisation potential of the considered ions are of order of maximally ~ 1 keV (the ionisation potentials are taken from Ref. [68]). Thus we can simply write the ion number densities as

$$n_{i,j} \approx n_i = \frac{\rho x_i}{m_i}. \tag{5.12}$$

Now we consider the partition functions given by Eq. (3.19) including the statistical weight $b_{i,j,k}$ and the excitation energies $\epsilon_{i,j,k}$. This part can be calculated by the schematic model constructed by K. Takahashi and K. Yokoi in Appendix B of Ref. [13]. They assumed that single-particle electrons fill up the electronic shells according to the serial order of the principal quantum number n and of the orbital quantum number l. Then the ground-state configuration can be specified by the quantum numbers of the last electron and the number of electrons N in this shell. In the end, the statistical weight is simply expressed by

$$b_{i,j,k} = \begin{cases} B_0(l,N) & \text{for } k = 0, \\ B_1(n,l,N) & \text{for } k = 1, \\ B_2(n,l,N,k) & \text{for } k > 0, \end{cases} \tag{5.13}$$

with

$$\begin{aligned} B_0(l,N) &= \frac{(2(2l+1))!}{N!(2(2l+1)-N)!}, \\ B_1(n,l,N) &= \frac{(2n^2)!}{(2l^2+N)!(2n^2-2l^2-N)!} - B_0(l,N), \\ B_2(n,l,N,k) &= \frac{2(n+k-1)^2(2n^2)!}{(2l^2+N-1)!(2n^2-2l^2-N+1)!}. \end{aligned} \tag{5.14}$$

Applying the H-like model formula to the outer bound excited electron, the excitation energies are obtained as:

$$\epsilon_{i,j,k} = \begin{cases} 0 & \text{for } k = 0 \text{ or } j = Z_i, \\ I_{i,j} - \frac{Ry(j+1)^2}{(n+k-1)^2} & \text{for } k \neq 0,\ j \neq Z_i, \end{cases} \tag{5.15}$$

where $I_{i,j}$ is the uncorrected ionisation potential, Z_i, the proton number of the atom i and Ry, the Rydberg unit of energy, $Ry = 13.60569253$ eV [69]. The cut-off integer for the summation in Eq. (3.19) is attained from the highest value for k that satisfies $\epsilon_{i,j,k} < I_{i,j} - \Delta_j$ where Δ_j accounts for the continuum depression correction [3].

In actual calculations, we have considered quantum corrections by treating electrons relativistically. The detailed treatment of electrons will not be discussed in this work. For more details, see Chapter 3 of Ref. [3].

5.2.3 Results

Before we solve the Saha equation, we first have to calculate the degeneracy parameter η and electron number density n_e. Consider the plasma Composition 1 at temperature $T_1 = 0.9 \times 10^8$ K, we can calculate n_e with Eq. (5.12):

$$n_e = \rho \sum_{i,j} j n_i = \rho \sum_i Z_i \frac{x_i}{m_i} = \rho\big(2\frac{x_{\mathrm{He}}}{m_{\mathrm{He}}} + 6\frac{x_{\mathrm{C}}}{m_{\mathrm{C}}} + 8\frac{x_{\mathrm{O}}}{m_{\mathrm{O}}}\big) = 3.00964 \times 10^{32}\ \mathrm{m}^{-3}. \tag{5.16}$$

By equalising the above value n_e with Eq. (3.13), we obtain

$$\eta = -2.62098. \tag{5.17}$$

Including the quantum corrections and ionisation potential corrections from the continuum depression, each ionisation state j from 1 to Z can be evaluated in a recurrence loop. The number density of a neutral atom is set to be 1. Summing over number densities of all possible ionisation states, and dividing the number density of ionisation state j by this sum, we can obtain the ionisation number fraction. Our results are listed in Tables 5.4 - 5.8, Figs. 5.2 and 5.3. The degrees of ionisation of selected isomers are summarised in Table 5.3.

As we can see from Table 5.3, atoms are more ionised in Composition 1 than in Composition 2, and are more ionised at the higher temperature T_2 than at T_1. Since our goal is to calculate the NEEC rates, we are particularly interested in vacancies of electronic shells in atoms so that free electrons can recombine. For the lower limit of the s-process temperature T_1, the average charge states range from approximately $(Z-5)$ (for ^{152}Eu with composition 2) to maximally Z (for ^{58}Co with Composition 1). At the higher temperature T_2, less than one bound electron is left on average, and this means that the L-shell is most likely vacant and the K-shell is partially vacant. With the information about charge states of atoms and their number density distributions in the plasmas, we can further calculate the NEEC rates. The results are presented in Section 5.3.

		Composition 1		Composition 2	
Isomer	Z	T_1	T_2	T_1	T_2
^{58}Co	27	26.2474	26.7709	25.8349	26.6476
^{99}Tc	43	40.6959	42.6194	39.8344	42.4598
^{121}Sn	50	46.8132	49.6010	45.8700	49.4314
^{124}Sb	51	47.7057	50.5978	46.7828	50.4264
^{152}Eu	63	58.6202	62.4004	58.0935	62.2016

Table 5.3: Degree of ionisation of selected isomers in the plasma Composition 1 and 2 (see table 2.2) at temperature T_1 and T_2.

Composition 1

Ionisation state j	≤ 22	23	24	25	26	27
T_1	$\leq$0.05	0.30	1.09	12.96	44.60	40.99
T_2	$\sim$0	$\sim$0	$\sim$0	0.52	21.85	77.62

Composition 2

Ionisation state j	≤ 22	23	24	25	26	27
T_1	$\leq$0.46	1.69	3.50	23.66	46.35	24.25
T_2	$\sim$0	$\sim$0	$\sim$0	1.13	30.24	68.62

Table 5.4: Distribution of ^{58}Co ion number densities in percent as function of the ionisation degree j at temperature $T_1 = 0.9 \times 10^8$ K and $T_2 = 0.48 \times 10^8$ K in the plasma Composition 1 and 2.

Composition 1

Ionisation state j	≤ 37	38	39	40	41	42	43
T_1	$\leq$ 0.96	4.65	12.92	17.98	36.58	22.61	4.30
T_2	$\sim$ 0	$\sim$0	$\sim$0	0.01	1.28	35.47	63.24

Composition 2

Ionisation state j	≤ 37	38	39	40	41	42	43
T_1	$\leq$0.55	16.78	26.72	21.31	24.86	8.81	0.96
T_2	$\sim$ 0	$\sim$0	$\sim$0	0.02	3.01	47.93	49.04

Table 5.5: Distribution of ^{99}Tc ion number densities in percent as function of the ionisation degree j at temperature $T_1 = 0.9 \times 10^8$ K and $T_2 = 0.48 \times 10^8$ K in the plasma Composition 1 and 2.

Composition 1								
Ionisation state j	≤ 43	44	45	46	47	48	49	50
T_1	$\leq$0.48	2.97	11.38	25.03	27.91	24.74	6.86	0.58
T_2	$\sim$0	~ 0	$\sim$0	$\sim$0	0.02	1.74	36.35	61.89
Composition 2								
Ionisation state j	≤ 43	44	45	46	47	48	49	50
T_1	$\leq$3.06	10.90	24.01	30.37	19.48	9.93	1.58	0.08
T_2	$\sim$0	~ 0	$\sim$0	0.01	0.09	4.04	48.49	47.38

Table 5.6: Distribution of ^{121}Sn ion number densities in percent as function of the ionisation degree j at temperature $T_1 = 0.9 \times 10^8$ K and $T_2 = 0.48 \times 10^8$ K in the plasma Composition 1 and 2.

Composition 1									
Ionisation state j	≤ 43	44	45	46	47	48	49	50	51
T_1	$\leq$0.06	0.57	3.39	12.51	26.48	28.50	22.59	5.51	0.40
T_2	$\sim$0	~ 0	$\sim$0	$\sim$0	$\sim$0	0.02	1.82	36.50	61.65
Composition 2									
Ionisation state j	≤ 43	44	45	46	47	48	49	50	51
T_1	$\leq$0.61	3.43	11.77	24.98	30.44	18.85	8.60	1.21	0.05
T_2	$\sim$0	~ 0	$\sim$0	$\sim$0	0.01	0.09	4.23	48.57	47.10

Table 5.7: Distribution of ^{124}Sb ion number densities in percent as function of the ionisation degree j at temperature $T_1 = 0.9 \times 10^8$ K and $T_2 = 0.48 \times 10^8$ K in the plasma Composition 1 and 2.

Composition 1

Ionisation state j	≤ 55	56	57	58	59	60	61	62	63
T_1	$\leq$0.30	1.83	13.93	28.89	33.09	18.33	3.49	0.10	$\sim$0
T_2	$\sim$0	$\sim$0	$\sim$0	$\sim$0	0.01	0.12	4.81	49.98	45.09

Composition 2

Ionisation state j	≤ 55	56	57	58	59	60	61	62	63
T_1	$\leq$2.63	9.35	19.12	24.09	32.67	10.47	1.15	0.02	$\sim$0
T_2	$\sim$0	$\sim$0	$\sim$0	$\sim$0	0.04	0.24	9.90	59.16	30.66

Table 5.8: Distribution of ^{152}Eu ion number densities in percent as function of the ionisation degree j at temperature $T_1 = 0.9 \times 10^8$ K and $T_2 = 0.48 \times 10^8$ K in the plasma Composition 1 and 2.

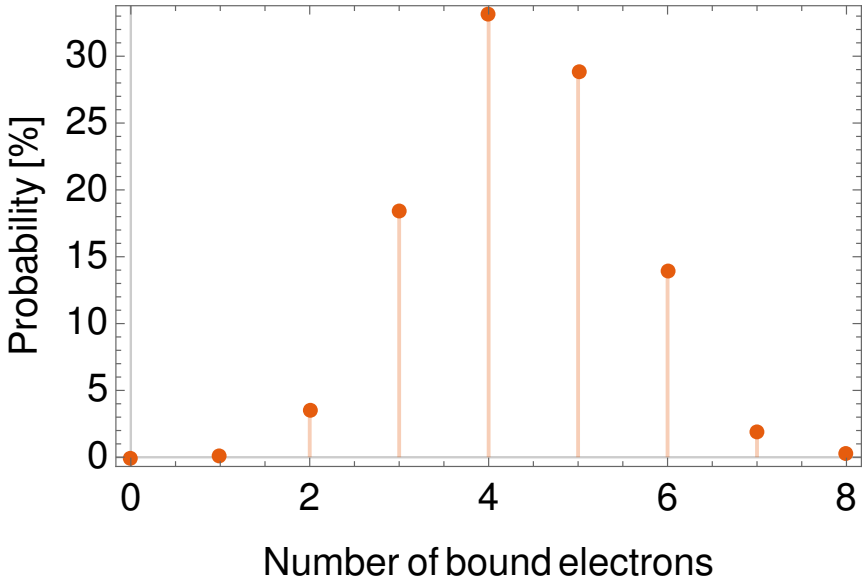

Figure 5.2: Ionisation states of ^{152}Eu in percent calculated from the Saha equation at temperature $T_1 = 0.9 \times 10^8$ K in the plasma Composition 1.

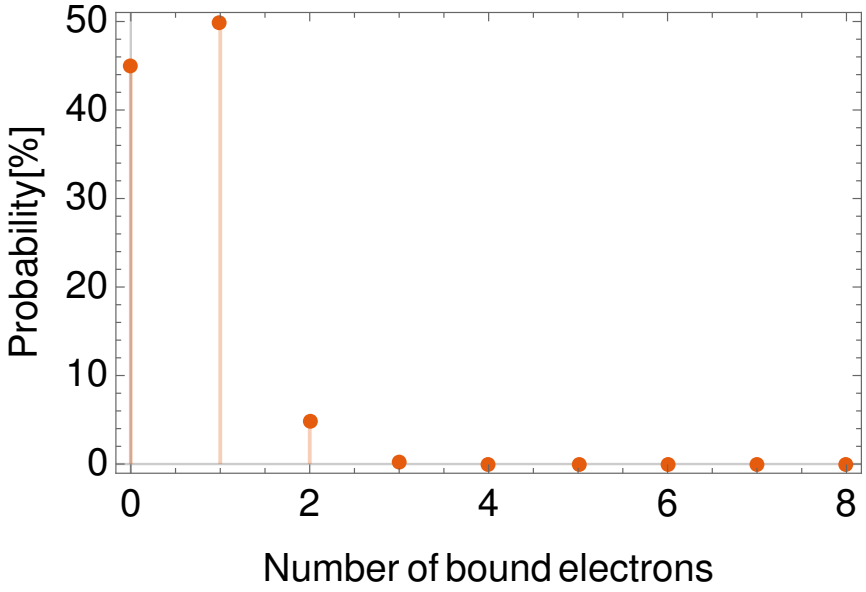

Figure 5.3: Ionisation states of ^{152}Eu in percent calculated from the Saha equation at temperature $T_2 = 3.48 \times 10^8$ K in the plasma Composition 1.

5.3 NEEC rates for nuclear transitions

The theoretical treatment of NEEC has been introduced in Chapter 4. The microscopic transition rates $Y_{\rm neec}$ are given in Eqs. (4.44) and (4.54), as

$$
\begin{aligned}
Y^{\mathcal{E}}_{\rm neec} &= \frac{4\pi^2\rho_i}{(2L+1)^2} R_0^{-2(L+2)} \mathcal{B}(\mathcal{E}L, I_{\rm i} \to I_{\rm d})(2j_{\rm d}+1) \sum_{\kappa} |R^{\mathcal{E}}_{L,\kappa_{\rm d},\kappa}|^2 C\left(j_{\rm d}\ L\ j; \frac{1}{2}\ 0\ \frac{1}{2}\right)^2, \\
Y^{\mathcal{M}}_{\rm neec} &= \frac{4\pi^2\rho_{\rm i}}{L^2(2L+1)^2} \mathcal{B}(\mathcal{M}L, I_{\rm i} \to I_{\rm d})(2j_{\rm d}+1) \\
&\qquad \times \sum_{\kappa} (2j+1)(\kappa_{\rm d}+\kappa) \begin{pmatrix} j_{\rm d} & j & L \\ \frac{1}{2} & -\frac{1}{2} & 0 \end{pmatrix}^2 |R^{\mathcal{M}}_{L,\kappa_{\rm d},\kappa}|^2.
\end{aligned}
\tag{5.18}
$$

To calculate the NEEC rates, one has to know the reduced nuclear transition probabilities $\mathcal{B}(\mathcal{E}L(\mathcal{M}L), I_{\rm i} \to I_{\rm d})$ and the integrals $R^{\mathcal{E}(\mathcal{M})}_{L,\kappa_{\rm d},\kappa}$ in Eqs. (4.45) and (4.55). The reduced nuclear transition probabilities and the energies of the nuclear transitions are taken from experimental data [67]. However, for the numerical integration of the electronic radial integrals, we have to know the bound and radial functions for the electrons. For the free electrons in the continuum, we use relativistic Coulomb-Dirac wave functions assuming that the nucleus is a point-like particle with effective charge $Z_{\rm eff} = q$ where q is the charge state of the ion. Since the free electron is far away from the nucleus, the internal structure or the size of the nucleus do not affect the behaviour of the free electron. Once the free electron is recombined to the nucleus, the electronic bound state is calculated by the *GRASP92 —General-purpose Relativistic Atomic Structure Program—* package [70]. This programme has been developed from 1980s to calculate relativistic atomic structures. For calculating atomic stationary states and transitions among stationary states, the multi-configuration Dirac-Fock (MCDF) method is used.
The nuclear radius R_0 is calculated from the semi-empirical formula [71]

$$
R_0 = (1.0793A^{1/3} + 0.73587)\ \text{fm}, \tag{5.19}
$$

where A denotes the atomic mass. First term of the radial integral in Eq. (4.45) is calculated to be 3 orders of magnitude smaller than the second term. This allows us to approximate $R^{\mathcal{E}}_{L,\kappa_{\rm d},\kappa}$ as

$$
R^{\mathcal{E}}_{L,\kappa_{\rm d},\kappa} \approx R_0^{L+2} \int_{R_0}^{\infty} dr_{\rm e} r_{\rm e}^{-L+1} \Big[f_{n_{\rm d}\kappa_{\rm d}}(r_{\rm e}) f_{\epsilon\kappa}(r_{\rm e}) + g_{n_{\rm d}\kappa_{\rm d}}(r_{\rm e}) g_{\epsilon\kappa}(r_{\rm e}) \Big]. \tag{5.20}
$$

This approximation is equivalent to the assumption that the electron is unlikely to be found inside the nuclear volume. With this assumption, the calculated NEEC cross section deviates by a few percent from the NEEC cross section that is rigorously calculated by the collective model without making any assumption about the motion of the electron [16].

5.3.1 Numerical results

We consider the electron recombining into different unoccupied levels in a given charge state. The bound electrons of ions are assumed to occupy the lowest level of electronic shells. The NEEC transition rates Y_{neec} are calculated first. Then the integrated cross section, the resonance strengths $S_{\mathrm{neec}}^{\mathrm{i}\to\mathrm{f}}$ for NEEC followed by the radiative or IC decay to the ground state are computed by using Eq. (4.35). The obtained two-step resonance strengths for all test isomers are listed from Table 5.9 to 5.13. Recombination to orbitals with angular momenta higher than 1 ($l > 1$) is also included in the net NEEC reaction rates but is only shown in Table 5.9.

The resonance strength is computed with different initial electron configurations—bare nucleus, H-like and He-like ions corresponding to zero, one, and two bound electrons left, since we saw in the previous Section that those are the most relevant for the considered plasma conditions. As we can see from Table 5.9, the resonance strength decreases for a fixed angular quantum number l while the principal quantum number n increases. This is a general behaviour of NEEC because the capture into deeply bound states is preferred. It can be best seen from the proportionality of resonance strength $S \sim \frac{1}{p^2}$ where p is the momentum of the recombining electron.

Additionally, we can observe from the calculated results in Table 5.9, that the resonance strength for a given capture channel decreases as the number of bound electrons increases. Once the number of bound electrons N_{bound} increases, the effective charge of the nucleus seen by the recombining electron decreases ($Z_{\mathrm{eff}} = Z - N_{\mathrm{bound}}$). Moreover, due to screening effects, the binding energy of a certain bound state becomes smaller if there are more bound electrons. A smaller binding energy results in a larger resonance energy E_{d} which consequently leads to smaller NEEC rates. Hence, NEEC is less likely and the resonance strength decreases. We can reasonably expect that the resonance strength continuously decreases as the number of initially bound electrons increases for lower charge state cases.

From the discussion of the s-process physical sites in Sec. 2.2, we know that T_2 is the most reasonable temperature for the s-process nucleosynthesis. Based on this, we have calculated the charge distribution of test isomers in Sec. 5.2. From the Saha results, we see that at T_2, most of ions are present in highly-charged states ($q \approx Z$) with only one or two bound electrons left (see Fig. 5.3 and Table from 5.4 to 5.8). Therefore, calculating the NEEC rates for the cases with up to two bound electrons will be sufficient for the NEEC reaction rates at T_2.

However, if we consider the lower temperature T_1 plasma, the distribution of charge states is broader (see Fig. 5.2). The percentage of lower charge states becomes significant ($\geq 30\%$). This means if we want to calculate the net NEEC rate λ_{neec} at T_1, we have to know the NEEC rates for lower charge states as well. Here, instead of calculating NEEC rates for all possible charge states, we estimate the NEEC rates in higher charge states from the calculated results for two bound electrons initially. Additionally, we exclude the capture levels which are occupied by bound electrons.

This estimation is valid because the difference of $S_{\mathrm{neec}}^{\mathrm{i}\to\mathrm{f}}$ by increasing one bound electron is maximally around 10% as seen from the numerical values in Table 5.9. Thus we are able

to provide a reasonable approximation by using the calculated two-bound-electron case for the lower charge cases. For calculating the NEEC reaction rate λ_{neec}, the obtained NEEC rates are weighted by the charge distribution obtained in Sec. 5.2. In this way, the uncertainty of the calculated NEEC reaction rates will be less than 10%. This argument is generally valid for all considered isomers.

N_{bound}	0	1	2
nl_j		$S_{\mathrm{neec}}^{\mathrm{i}\to\mathrm{f}}$ (barn·eV)	
$1s_{1/2}$	8.331×10^{-7}	7.975×10^{-7}	-
$2s_{1/2}$	1.558×10^{-7}	1.451×10^{-7}	1.388×10^{-7}
$2p_{1/2}$	1.121×10^{-7}	1.030×10^{-7}	9.177×10^{-8}
$2p_{3/2}$	2.136×10^{-7}	1.959×10^{-7}	1.740×10^{-7}
$3s_{1/2}$	5.769×10^{-8}	5.264×10^{-8}	4.957×10^{-8}
$3p_{1/2}$	4.406×10^{-8}	3.975×10^{-8}	3.489×10^{-8}
$3p_{3/2}$	8.379×10^{-8}	7.550×10^{-8}	6.608×10^{-8}
$3d_{3/2}$	7.969×10^{-10}	6.478×10^{-10}	5.184×10^{-10}
$3d_{5/2}$	1.066×10^{-9}	8.698×10^{-10}	6.980×10^{-10}
$4s_{1/2}$	2.610×10^{-8}	2.358×10^{-8}	2.202×10^{-8}
$4p_{1/2}$	2.040×10^{-8}	1.826×10^{-8}	1.592×10^{-8}
$4p_{3/2}$	3.881×10^{-8}	3.468×10^{-8}	3.016×10^{-8}
$4d_{3/2}$	4.514×10^{-10}	3.683×10^{-10}	2.957×10^{-10}
$4d_{5/2}$	6.044×10^{-10}	4.947×10^{-10}	3.983×10^{-10}
$4f_{5/2}$	5.981×10^{-12}	4.524×10^{-12}	3.376×10^{-12}
$4f_{7/2}$	7.263×10^{-12}	5.502×10^{-12}	4.112×10^{-12}
$5s_{1/2}$	1.369×10^{-8}	1.231×10^{-8}	1.144×10^{-8}
$5p_{1/2}$	1.084×10^{-8}	9.666×10^{-9}	8.405×10^{-9}
$5p_{3/2}$	2.064×10^{-8}	1.837×10^{-8}	1.593×10^{-8}
$5d_{3/2}$	2.585×10^{-10}	2.112×10^{-10}	1.699×10^{-10}
$4d_{5/2}$	3.463×10^{-10}	2.839×10^{-10}	2.289×10^{-10}
$5f_{5/2}$	4.815×10^{-12}	3.649×10^{-12}	2.729×10^{-12}
$5f_{7/2}$	5.840×10^{-12}	4.433×10^{-12}	3.320×10^{-12}
$5g_{7/2}$	2.663×10^{-14}	1.840×10^{-14}	1.264×10^{-14}
$5g_{9/2}$	3.081×10^{-14}	2.141×10^{-14}	1.481×10^{-14}

Table 5.9: Two step resonance strengths $S_{\mathrm{neec}}^{\mathrm{i}\to\mathrm{f}}$ for ^{58}Co with different ionic configurations involving $M1 + E2$ nuclear transitions (as illustrated in Fig. 5.1). NEEC is followed by the radiative and IC decay to the ground state. nl_j indicates the capture orbital.

N_{bound}	0	1	2
nl_j		$S^{\text{i}\to\text{f}}_{\text{neec}}$ (barn·eV)	
$4s_{1/2}$	6.576×10^{-18}	5.939×10^{-18}	5.286×10^{-18}
$4p_{1/2}$	1.526×10^{-17}	1.352×10^{-17}	1.216×10^{-17}
$4p_{3/2}$	2.947×10^{-17}	2.632×10^{-17}	2.375×10^{-17}
$5s_{1/2}$	2.391×10^{-18}	2.311×10^{-18}	2.171×10^{-18}
$5p_{1/2}$	7.528×10^{-18}	7.232×10^{-18}	6.964×10^{-18}
$5p_{3/2}$	1.492×10^{-17}	1.436×10^{-17}	1.383×10^{-17}

Table 5.10: Two step resonance strengths $S^{\text{i}\to\text{f}}_{\text{neec}}$ for ^{99}Tc with different ionic configurations involving $E3$ nuclear transitions (as illustrated in Fig. 5.1). NEEC is followed by the radiative and IC decay to the ground state. nl_j indicates the capture orbital.

N_{bound}	0	1	2
nl_j		$S^{\text{i}\to\text{f}}_{\text{neec}}$ (barn·eV)	
$3s_{1/2}$	3.063×10^{-20}	2.565×10^{-20}	2.169×10^{-20}
$3p_{1/2}$	9.559×10^{-22}	8.366×10^{-22}	7.318×10^{-22}
$3p_{3/2}$	9.579×10^{-19}	7.889×10^{-19}	6.386×10^{-19}
$4s_{1/2}$	1.172×10^{-20}	1.005×10^{-20}	8.692×10^{-21}
$4p_{1/2}$	4.689×10^{-22}	4.150×10^{-22}	3.663×10^{-22}
$4p_{3/2}$	3.116×10^{-19}	2.648×10^{-19}	2.211×10^{-19}
$5s_{1/2}$	6.002×10^{-21}	5.171×10^{-21}	4.487×10^{-21}
$5p_{1/2}$	2.627×10^{-22}	2.325×10^{-22}	2.051×10^{-22}
$5p_{3/2}$	1.499×10^{-19}	1.283×10^{-19}	1.078×10^{-19}

Table 5.11: Resonance strengths $S^{\text{i}\to\text{f}}_{\text{neec}}$ for ^{121}Sn with different ionic configurations involving $M4$ nuclear transitions (as illustrated in Fig. 5.1). NEEC is followed by the radiative and IC decay to the ground state. nl_j indicates the capture orbital.

N_{bound}	0	1	2
nl_j		$S_{\text{neec}}^{\text{i}\to\text{f}}$ (barn·eV)	
$2s_{1/2}$	1.388×10^{-7}	1.249×10^{-7}	1.217×10^{-7}
$2p_{1/2}$	1.832×10^{-6}	1.725×10^{-6}	1.605×10^{-6}
$2p_{3/2}$	3.190×10^{-6}	2.951×10^{-6}	2.735×10^{-6}
$3s_{1/2}$	3.771×10^{-8}	3.406×10^{-8}	3.284×10^{-8}
$3p_{1/2}$	6.210×10^{-7}	5.825×10^{-7}	5.406×10^{-7}
$3p_{3/2}$	1.068×10^{-6}	9.992×10^{-7}	9.232×10^{-7}
$4s_{1/2}$	1.545×10^{-8}	1.396×10^{-8}	1.339×10^{-8}
$4p_{1/2}$	2.747×10^{-7}	2.569×10^{-7}	2.378×10^{-7}
$4p_{3/2}$	4.734×10^{-7}	4.415×10^{-7}	4.069×10^{-7}
$5s_{1/2}$	7.806×10^{-9}	7.049×10^{-9}	6.754×10^{-9}
$5p_{1/2}$	1.428×10^{-7}	1.333×10^{-7}	1.233×10^{-7}
$5p_{3/2}$	2.468×10^{-7}	2.298×10^{-7}	2.116×10^{-7}

Table 5.12: Two step resonance strengths $S_{\text{neec}}^{\text{i}\to\text{f}}$ for ^{124}Sb with different ionic configurations involving $E1$ nuclear transitions (as illustrated in Fig. 5.1). NEEC is followed by the radiative and IC decay to the ground state. nl_j indicates the capture orbital.

N_{bound}	0	1	2
nl_j		S_{neec} (barn·eV)	
$2s_{1/2}$	1.318×10^{-5}	1.228×10^{-5}	1.138×10^{-5}
$2p_{1/2}$	1.721×10^{-5}	1.483×10^{-5}	1.270×10^{-5}
$2p_{3/2}$	4.233×10^{-6}	3.711×10^{-6}	3.199×10^{-6}
$3s_{1/2}$	4.266×10^{-6}	4.149×10^{-6}	4.033×10^{-6}
$3p_{1/2}$	2.153×10^{-6}	1.978×10^{-6}	1.801×10^{-6}
$3p_{3/2}$	4.795×10^{-7}	4.431×10^{-7}	4.046×10^{-7}
$4s_{1/2}$	2.688×10^{-6}	2.598×10^{-6}	2.513×10^{-6}
$4p_{1/2}$	7.577×10^{-7}	7.003×10^{-7}	6.422×10^{-7}
$4p_{3/2}$	1.550×10^{-7}	1.448×10^{-7}	1.340×10^{-7}
$5s_{1/2}$	1.789×10^{-6}	1.713×10^{-6}	1.643×10^{-6}
$5p_{1/2}$	3.591×10^{-7}	3.327×10^{-7}	3.059×10^{-7}
$5p_{3/2}$	7.071×10^{-8}	6.637×10^{-8}	6.174×10^{-8}

Table 5.13: Two step resonance strengths $S_{\text{neec}}^{\text{i}\to\text{f}}$ for ^{152}Eu with different ionic configurations involving $M1$ nuclear transitions (as illustrated in Fig. 5.1). NEEC is followed by the radiative and IC decay to the ground state. nl_j indicates the capture orbital.

5.4 Total NEEC reaction rates

The three main ingredients for the final NEEC reaction rate calculation are prepared: the NEEC resonance strength S_{neec}, the charge state distribution of ions in the plasma, and the resonant electron flux $\phi_{\mathrm{e}}(E_{\mathrm{d}})$. The charge distribution of ions is computed in Sec. 5.2. The resonance strength is calculated for NEEC followed by radiative and IC decay to the ground state. The calculated resonance strengths and the estimation used for the low charge cases have been discussed in Sec. 5.3. Finally, the resonant electron flux is evaluated by integrating the Fermi-Dirac distribution given by Eq. (5.2). The resonant electron fluxes in the plasma Composition 1 at T_1 and T_2 for ^{152}Eu are shown in Table. 5.14.

nl_j	E_{d} (keV)	S_{neec} (barn·eV)	Φ_1^{res} $(1/\mathrm{m}^2/\mathrm{s}/\mathrm{eV})$	Φ_2^{res} $(1/\mathrm{m}^2/\mathrm{s}/\mathrm{eV})$
$2\mathrm{s}_{1/2}$	5.959	1.138×10^{-5}	7.902×10^{35}	1.705×10^{35}
$2\mathrm{p}_{1/2}$	6.109	1.270×10^{-5}	7.952×10^{35}	1.740×10^{35}
$2\mathrm{p}_{3/2}$	6.840	3.199×10^{-6}	8.132×10^{35}	1.903×10^{35}
$3\mathrm{s}_{1/2}$	13.705	4.033×10^{-6}	6.886×10^{35}	3.057×10^{35}
$3\mathrm{p}_{1/2}$	13.746	1.801×10^{-6}	6.871×10^{35}	3.062×10^{35}
$3\mathrm{p}_{3/2}$	13.964	4.046×10^{-7}	6.791×10^{35}	3.089×10^{35}
$4\mathrm{s}_{1/2}$	16.369	2.513×10^{-6}	5.870×10^{35}	3.351×10^{35}
$4\mathrm{p}_{1/2}$	16.386	6.422×10^{-7}	5.863×10^{35}	3.353×10^{35}
$4\mathrm{p}_{3/2}$	16.477	1.340×10^{-7}	5.828×10^{35}	3.362×10^{35}
$5\mathrm{s}_{1/2}$	17.585	1.643×10^{-6}	5.404×10^{35}	3.362×10^{35}
$5\mathrm{p}_{1/2}$	17.594	3.059×10^{-7}	5.401×10^{35}	3.364×10^{35}
$5\mathrm{p}_{3/2}$	17.640	6.174×10^{-8}	5.383×10^{35}	3.467×10^{35}

Table 5.14: Resonance strength S_{neec} for ^{152}Eu with two bound electrons (i.e., He-like ionic configuration) involving $M1$ nuclear transitions (as illustrated in Fig. 5.1). E_{d} is the energy of the free electron at the resonance, nl_j, the capture orbital, Φ_1^{res} and Φ_2^{res} are the resonant electron fluxes at T_1 and T_2 with Composition 1, respectively.

For calculating the reaction rates λ_{neec}, we have to put the resonance strength and resonant electron flux together and then sum over possible charge states and capture channels. However, taking all possible charge states and capture channels into account is not realistic and time-consuming. Therefore, we need to introduce an atomic "cut-off" level to calculate λ_{neec} efficiently.

As discussed in Sec. 5.3, the resonant strength decreases for increasingly less bound capture shells. For instance, the resonance strength for capture into $2s_{1/2}$ is higher than that for capture into $5s_{1/2}$ by a factor of 10 in Table 5.14. Therefore, it is reasonable to consider the resonance strength up to O-shell ($n = 5$), since the resulting uncertainty will be on the level of 10%.

In the next step, we examine if this cut-off is suitable for the electron flux or not. The

electron flux $\phi_e(E)$ is calculated by Eq. (5.2) which is close to a Maxwell-Boltzmann distribution with a peak at around $E \sim k_B T$. If electron energies are distributed before the peak, i.e., $E < k_B T$, the electron flux increases as the electron energy increases. On the other hand, if electron energies are distributed after the peak, i.e., $E > k_B T$, the electron flux decreases as the electron energy increases. We have considered two different temperatures T_1 and T_2, the corresponding thermal energies are $k_B T_1 \approx 8$ keV and $k_B T_2 \approx 30$ keV, respectively. The resonant energy E_d decreases for the considered bound capture shells in Table 5.14. First, we consider the low temperature case, T_1. The electron flux increases for first three shells ($E_\mathrm{d} < k_B T_1$) but later, it starts to decrease for the rest ($E_\mathrm{d} > k_B T_1$). Indeed, the cut-off level is valid at T_1. Then, we consider the resonant flux at T_2. From Table 5.14, we see that the electron flux increases for less bound capture shells since $E_\mathrm{d} < k_B T_2$. However, the resonant electron flux for capture into $5s_{1/2}$ is higher than that for capture into $2s_{1/2}$ only by a factor of 2, i.e., the resonant electron fluxes at two different temperatures are still in the same order of magnitude. If the resonance strength decreases faster than the electron flux, the atomic cut-off is still applicable. The results are presented for s and p orbitals in Table 5.14, but the net reaction rate λ_neec includes all possible orbitals from $n = 1$ to $n = 5$. Energy levels of the given isomers are always of the order of $(1 \sim 10)$ keV. This will result in approximately the same order of the E_d values for the rest of isomers and we assume that similar arguments can be applied for the other isomers. Consequently, we can safely choose $5g_{9/2}$ as our atomic cut-off level for calculating λ_neec.

Plugging the calculated charge state distribution, NEEC rates and electron flux together, we eventually obtain the net reaction rate in the plasma. The obtained results are summarised in Table 5.15.

	λ_neec (1/s)			
Plasma conditions	T_1, C_1	T_1, C_2	T_2, C_1	T_2, C_2
^{58}Co	1.978×10	3.371×10	3.069×10	5.292×10
^{99}Tc	5.034×10^{-9}	8.468×10^{-9}	7.167×10^{-10}	1.237×10^{-9}
^{121}Sn	8.728×10^{-11}	1.477×10^{-10}	1.955×10^{-11}	3.303×10^{-11}
^{124}Sb	2.393×10^{2}	4.044×10^{2}	2.983×10^{2}	5.128×10^{2}
^{152}Eu	2.044×10^{3}	3.124×10^{3}	9.176×10^{2}	1.576×10^{3}

Table 5.15: The net NEEC reaction rates in the plasma for the selected isomers. T_1, T_2 denote the plasma temperature conditions and C_1, C_2 denote the plasma Composition 1 and 2.

The reaction rates of ^{99}Tc and ^{121}Sn are almost ten orders of magnitude lower than those of ^{58}Co, ^{124}Sb and ^{152}Eu. This is reasonable, since the considered electromagnetic transitions for ^{99}Tc and ^{121}Sn are $E3\&M4$, and are $E1$,$E2\&M1$ for the rest of the isomers. The transition rate decreases significantly with the increasing multipolarity L. The reaction rates of ^{124}Sb and ^{152}Eu show the highest values among ones from all

selected candidates.

Now we compare the reaction rates for a given isomer. If the Composition is fixed, the reaction rate is higher at the higher temperature T_2. Following the argument discussed in Sec. 5.3, the higher temperature condition results in higher charge states, which leads to an increase of effective charge, binding energy and hence the resonance strength. Since the reaction rate is proportional to the resonance strength, the reaction rate increases.

If the temperature is fixed, the reaction rate is higher in the plasma Composition 2 than that in Composition 1. In principle, this can also be explained by the same argument, however, the charge state distributions are not distinctive between two Compositions (see Tables from 5.4 to 5.8). We know that the electron density is calculated by Eq. (5.9) and the plasma Compositions 1 and 2 have different electron densities. For this reason, we suspect that the electron density plays a major role here.

Isomer	τ_{neec} (s)	τ_m (s)	Decay channel
^{58}Co	$\approx 10^{-2}$	$\approx 4.8 \times 10^3$	$\gamma(100\%)$
^{99}Tc	$\approx 10^{9}$	$\approx 3.8 \times 10^3$	$\gamma(99.9963\%)$, $\beta^-(0.0037\%)$
^{121}Sn	$\approx 10^{10}$	$\approx 2.0 \times 10^9$	$\gamma(77.6\%)$, $\beta^-(22.4\%)$
^{124}Sb	$\approx 10^{-3}$	$\approx 1.3 \times 10^2$	$\gamma(75\%)$, $\beta^-(25\%)$
^{152}Eu	$\approx 10^{-4}$	$\approx 4.8 \times 10^3$	EC+$\beta^+(27\%)$, $\beta^-(73\%)$

Table 5.16: Comparison of the half-lives and NEEC time scales for the test isomers. The NEEC time scales are estimated by taking the inverse of averaged λ_{neec} from Table 5.15. The half-lives of isomers are taken from Ref. [67]. EC denotes the electron capture, γ, the gamma-decay, and β, the beta-decay, respectively.

Finally, we compare the obtained NEEC time scale with the relevant isomeric weak and electromagnetic decay times in Table 5.16. Our numerical results show that the NEEC time scales are several orders of magnitude faster than the gamma and beta decay times for ^{58}Co, ^{124}Sb and ^{152}Eu. This means that isomers would rather decay by NEEC than by beta- or gamma-decays. NEEC can efficiently depopulate isomeric states under *s*-process nucleosynthesis conditions. Possibly, the lifetime of the isomer is shortened via NEEC. We conclude that NEEC should be considered as a relevant isomer depletion channel in astrophysical plasmas.

It is probable that in *s*-process nucleosynthesis scenarios, the decay chain of the nuclei might be influenced by the decay of the isomer via NEEC; the Maxwell-Boltzmann distribution of the nuclei can be reached even faster, because of the shortened isomeric lifetime via NEEC.

However, in order to examine the last point we need to set up a set of rate equations including the corresponding rates. Then we can keep track of nuclear populations in time and see if the decay via NEEC plays an important role. This calls for further research.

Summary and Outlook

In this thesis, we have theoretically investigated the efficiency of NEEC to depopulate isomeric states under the *s*-process conditions. Nuclear isomers are often not thermalised with the rest of the nuclear excited states in astrophysical environments and must be treated as additional nuclear species in the nucleosynthesis nuclear reaction networks. The NEEC depletion mechanism has received little attention so far, partly because under LTE assumptions, the exact excitation and decay mechanisms are not considered separately. However, our first qualitative estimates show that in the case of NEEC, the inverse process is often forbidden, rendering NEEC reaction rates for the depletion of isomers relevant.

We have calculated NEEC reaction rates under the *s*-process conditions for a selection of isomers with astrophysical relevance, namely ^{58m}Co, ^{99m}Tc, ^{121m}Sn, ^{124m}Sb, and ^{152m}Eu. The calculation is divided into three parts. First, we have obtained the charge state distributions of the ions of interest in the plasma under stellar conditions by solving numerically the Saha equation. This is performed for two plasma compositions and two temperature values relevant for *s*-process nucleosynthesis. As a second step, we have calculated the NEEC rates for recombination into several vacant orbitals of the ions in the plasma.

To this end, we have computed relativistic bound and continuum electronic wave functions using the multi-configurational Dirac Fock method implemented in the GRASP92 code and Coulomb-Dirac routines, respectively. Finally, as a third step the NEEC resonance strengths were integrated over the electron flux in the plasma to obtain the actual reaction rates for the specific astrophysical conditions considered.

We have compared the obtained NEEC rates with the relevant isomeric weak and electromagnetic decay rates that determine the thermalisation time-scale for the isomeric state. Our numerical results show that the NEEC reaction rates for ^{58m}Co, ^{124m}Sb, and ^{152m}Eu are faster than beta and gamma decay rates of isomeric states. This confirms that NEEC can be an efficient depletion channel for isomeric states under *s*-process nucleosynthesis conditions and should be investigated in more detail. As an outlook, more detailed calculations for a larger list of case study isomers should be performed.

Our work can also be made the subject of further refinements. Presently used approximations could be improved. For instance, for the lower plasma temperature the NEEC rates for recombination into ions with charges lower than He-like were approximated from the corresponding rates for capture into He-like ions. We expect this approximation to produce uncertainties on the level of 10%. More detailed calculations for the actual conditions in the plasma could be performed. On the other hand, one could attempt to include the expected degeneracy effects due to the plasma environment for the bound and continuum electronic wave functions, which are in the present work not including

any plasma effects.

Finally, a further direction could include a self-consistently calculation of the thermalisation of the isomeric states taking into account NEEC together with the partially closed IC channels and purely electronic processes such as collisional and photo-ionisation. At present, the discussion concerning thermalisation of the isomeric states was only based on qualitative arguments about NEEC, IC and collisional ionisation. The thermalisation time-scale could be however deduced quantitatively by taking into account all relevant atomic and nuclear processes.

List of Figures

List of Tables

Bibliography

[1] J. J. Cowan and F. Thielemann. r-process nucleosynthesis in supernovae. *Physics Today*, October, 2004.

[2] W. A. Fowler E. M. Burbidge, G. R. Burbidge and F. Hoyle. Synthesis of the elements in stars. *Rev. Mod. Phys.*, 29(4), 1957.

[3] K. Beckerle. *Ionisation of Osmium in a stellar plasma under s-process conditions.* Bachelor's thesis, Universität Heidelberg, 2012.

[4] M. R. Harston and J. F. Chemin. Mechanisms of nuclear excitation in plasmas. *Phys. Rev. C*, 59(5), 1999.

[5] G. Gosselin and P. Morel. Enhanced nuclear level decay in hot dense plasmas. *Phys. Rev. C*, 70(064603), 2004.

[6] V. Méot G. Gosselin and P. Morel. Modified nuclear level lifetime in hot dense plasmas. *Phys. Rev. C*, 76(044611), 2007.

[7] P. Morel G. Gosselin and P. Mohr. Modification of nuclear transitions in stellar plasma by electronic processes: K-isomers in 176lu and 180ta under s-process conditions. *Phys. Rev. C*, 81(055808), 2010.

[8] R. A. Ward. The importance of long-lived isomeric states in s-process branching. *Astrophys. J.*, 216, 1977.

[9] R. A. Ward. Stellar ion-induced Coulomb enhancements of nuclear radiative decay rates. *Astro. & Astrophys.*, 97:157–168, April 1981.

[10] Z.Y. Bao and F. Kaeppeler. Neutron capture cross sections for s-process studies. *At. Data Nucl. Data Tables; (United States)*, 36:3, May 1987. doi: 10.1016/0092-640X(87)90011-8.

[11] V. L. Peterson and D. A. Tripp. Determination of the s-process neutron capture time. *Astrophys. J.*, 184, 1973.

[12] K. Takahashi and K. Yokoi. Beta-decay rates of highly ionized heavy atoms in stellar interiors. *Atomic data and nuclear data tables*, 36, 1987.

[13] K. Takahashi and K. Yokoi. Nuclear β-decays of highly ionized heavy atoms in stellar interiors. *Nuclear Physics A*, 404:578–598, August 1983. doi: 10.1016/0375-9474(83)90277-4.

[14] R. A. Ward and W. A. Fowler. Thermalization of long-lived nuclear isomeric states under stellar conditions. *Astrophys. J.*, 238, 1980.

[15] V. I. Goldanskii and V. A. Namiot. On the excitation of isomeric nuclear levels by laser radiation through inverse internal electron conversion. *Phys. Lett. B*, 62(4), 1976.

[16] A. Pálffy. *Theory of nuclear excitation by electron capture for heavy ions.* PhD dissertation, Justus-Liebig-Universität Gießen, 2006.

[17] J. C. Poizat N. Cue and J. Remillieux. Exciting the nucleus by target electron capture into atomic orbitals. *Europhys. Lett.*, 8(1), 1989.

[18] N. Cue. Nuclear excitation by target electron capture. *Nuclear Instruments and Methods in Physics Research Section B*, 40-41, 1989.

[19] D. Bittel J. C. Kimball and N. Cue. A comment on "nuclear excitation by target electron capture". *Physics Letters A*, 152(7), 1991.

[20] Zhu-Shu Yuan and J. C. Kimball. First-principles calculation of the cross sections for nuclear excitation by electron capture of channeled nuclei. *Phys. Rev. C*, 47(1), 1993.

[21] M. N. Saha. Ionization in the solar chromosphere. *Philosophical Magazine*, 6, 1920.

[22] G. Elert, The Physics Hypertextbook, 1998-2017. URL http://physics.info/.

[23] H. Schatz. Rare isotopes in the cosmos. *Physics Today*, November, 2008.

[24] Christopher Sneden and John J. Cowan. Genesis of the heaviest elements in the milky way galaxy. *Science*, 299(5603):70–75, 2003. ISSN 0036-8075. doi: 10.1126/science.1077506. URL http://science.sciencemag.org/content/299/5603/70.

[25] K. Langanke. Nuclear astrophysics: selected topics. *Lect. Notes Phys.*, 652, 2004.

[26] F. Käppler. The origin of the heavy elements: The *s*-process. *Prog. Part. Nucl. Phys.*, 43, 1999.

[27] P. Parker A. M. Boesgaard G. M. Hale A. E. Champagne C. A. Barnes F. Käppler V. V. Smith R. D. Hoffman F. X. Timmes C. Sneden R. N. Boyd B. S. Meyer G. Wallerstein, I. Iben and D. L. Lambert. Synthesis of the elements in stars: forty years of progress. *Rev. Mod. Phys.*, 69(4), 1997.

[28] S. Bisterzo F. Käppeler, R. Gallino and W. Aoki. The *s*-process: Nuclear physics, stellar models, and observations. *Rev. Mod. Phys.*, 83, 2011.

[29] M. Busso G. Picchio F. Käppler, R. Gallino and C. M. Raiteri. S-process nucleosynthesis - classical approach and asymptotic giant branch models for low-mass stars. *Astrophys. J.*, 354, 1990.

[30] F. Käppeler K. A. Toukan, K. Debus and G. Reffo. Stellar neutron capture cross sections of nd, pm, and sm isotopes. *Phys. Rev. C*, 51(3), 1995.

[31] F. Käppeler G. Walter, H. Beer and R. D. Penzhorn. The s-process branching at kr-85. *Astron. Astrophys.*, 155(2), 1986.

[32] F. Käppeler G. Reffo G. Walter, H. Beer and F. F. Fabbri. The s-process branching at se-79. *Astron. Astrophys.*, 167(1), 1986.

[33] S. Jaag F. Käppeler C. Doll, H. G. Börner and W. Andrejtscheff. Lifetime measurement in 176lu and its astrophysical consequences. *Phys. Rev. C*, 59, 1999.

[34] K. Wisshak, K. Guber, F. Voss, F. Käppeler, and G. Reffo. Neutron capture in ^{148,150}Sm: A sensitive probe of the s-process neutron density. *Phys. Rev. C*, 48: 1401–1419, Sep 1993. doi: 10.1103/PhysRevC.48.1401. URL http://link.aps.org/doi/10.1103/PhysRevC.48.1401.

[35] K. Wisshak, F. Voss, F. Käppeler, K. Guber, L. Kazakov, N. Kornilov, M. Uhl, and G. Reffo. Stellar neutron capture cross sections of the gd isotopes. *Phys. Rev. C*, 52:2762–2779, Nov 1995. doi: 10.1103/PhysRevC.52.2762. URL http://link.aps.org/doi/10.1103/PhysRevC.52.2762.

[36] S. Jaag and F. Kaeppeler. The Stellar (n, gamma) Cross Section of the Unstable Isotope 163Ho and the Origin of 164Er. *Astrophys. J.*, 464:874, June 1996. doi: 10.1086/177375.

[37] N. Klay, F. Käppeler, H. Beer, and G. Schatz. Nuclear structure of ^{176}Lu and its astrophysical consequences. ii. ^{176}Lu, a thermometer for stellar helium burning. *Phys. Rev. C*, 44:2839–2849, Dec 1991. doi: 10.1103/PhysRevC.44.2839. URL http://link.aps.org/doi/10.1103/PhysRevC.44.2839.

[38] F. Kaeppeler, W. Schanz, K. Wisshak, and G. Reffo. The s-process between A = 120 and 124 - Signature of neutron density and temperature in red giants. *Astrophys. J.*, 410:370–386, June 1993. doi: 10.1086/172754.

[39] F. Voss, K. Wisshak, K. Guber, F. Käppeler, and G. Reffo. Stellar neutron capture cross sections of the ba isotopes. *Phys. Rev. C*, 50:2582–2601, Nov 1994. doi: 10.1103/PhysRevC.50.2582. URL http://link.aps.org/doi/10.1103/PhysRevC.50.2582.

[40] P. E. Koehler, R. R. Spencer, R. R. Winters, K. H. Guber, J. A. Harvey, N. W. Hill, and M. S. Smith. Resonance neutron capture and transmission measurements and the stellar neutron capture cross sections of ^{134}Ba and ^{136}Ba. *Phys. Rev. C*, 54:1463–1477, Sep 1996. doi: 10.1103/PhysRevC.54.1463. URL http://link.aps.org/doi/10.1103/PhysRevC.54.1463.

[41] F. Kaeppeler, S. Jaag, Z. Y. Bao, and G. Reffo. The s-process branchings at W-185 and Re-186. *Astrophys. J.*, 366:605–616, January 1991. doi: 10.1086/169596.

[42] J. C. Lattanzio R. Gallino M. Lugaro, F. Herwig and O. Straniero. s-process nucleosynthesis in asymptotic giant branch stars: A test for stellar evolution. *The Astrophysical Journal*, 586(2):1305, 2003. URL http://stacks.iop.org/0004-637X/586/i=2/a=1305.

[43] F. Herwig. Evolution of asymptotic giant branch stars. *Annual Review of Astronomy and Astrophysics*, 43(1):435–479, 2005. doi: 10.1146/annurev.astro.43.072103.150600. URL http://dx.doi.org/10.1146/annurev.astro.43.072103.150600.

[44] Magnus Vilhelm Persson. Proposed internal structure of AGB star. 8 2014. doi: 10.6084/m9.figshare.653683.v2. URL https://figshare.com/articles/Internal_structure_of_AGB_star/653683.

[45] R. Gallino, C. Arlandini, M. Busso, M. Lugaro, C. Travaglio, O. Straniero, A. Chieffi, and M. Limongi. Evolution and Nucleosynthesis in Low-Mass Asymptotic Giant Branch Stars. II. Neutron Capture and the S-Process. *The Astrophysical Journal*, 497:388–403, April 1998. doi: 10.1086/305437.

[46] A. I. Boothroyd and I.-J. Sackmann. Low-Mass Stars. III. Low-Mass Stars with Steady Mass Loss: Up to the Asymptotic Giant Branch and through the Final Thermal Pulses. *The Astrophysical Journal*, 328:653, May 1988. doi: 10.1086/166323.

[47] J. P. Cox and R. T. Giuli. *Principles of stellar structure*. Gordon and Breach, 1968.

[48] Ewa Niemczura, Barry Smalley, and Wojtek Pych, editors. *NLTE Radiative Transfer in Cool Stars*, pages 169–185. Springer International Publishing, Cham, 2014. ISBN 978-3-319-06956-2. doi: 10.1007/978-3-319-06956-2_16. URL http://dx.doi.org/10.1007/978-3-319-06956-2_16.

[49] G. W. Collins. *The fundamentals of stellar astrophysics*. W.H. Freeman, 1989.

[50] L. Neise W. Greiner and H. Stöcker. *Thermodynamics and statistical mechanics*, chapter 13-14. Springer, 1997.

[51] A. G. W. Cameron. Neutron star models. *Astrophys. J.*, 130, 1959.

[52] M. J. Newman R. A. Ward and D. D. Clayton. S-process studies: branching and the time scale. *Astrophys. J. Suppl.*, 31, 1976.

[53] G. R. Caughlan W. A. Fowler and B. A. Zimmerman. Thermonuclear reaction rates. *Ann. Rev. Astr. Ap.*, 13(69), 1975.

[54] S. B. Solomon and D. G. Sargood. Stellar reaction rates for $^{45}\mathrm{Sc}(p,\gamma)^{46}\mathrm{Ti}$. *Astrophys. J.*, 223, 1978.

[55] M. Hegelich, S. Karsch, G. Pretzler, D. Habs, K. Witte, W. Guenther, M. Allen, A. Blazevic, J. Fuchs, J. C. Gauthier, M. Geissel, P. Audebert, T. Cowan, and M. Roth. Mev ion jets from short-pulse-laser interaction with thin foils. *Phys. Rev. Lett.*, 89:085002, Aug 2002. doi: 10.1103/PhysRevLett.89.085002. URL http://link.aps.org/doi/10.1103/PhysRevLett.89.085002.

[56] J. Gunst. *Mutual control of x-rays and nuclear transitions*. PhD dissertation, Universität Heidelberg, 2015.

[57] S. Trotsenko G. Plunien Th. Stöhlker A. V. Volotka, A. Surzhykov and S. Fritzsche. Nuclear excitation by two-photon electron transition. *Phys. Rev. Lett.*, 117(243001), 2016.

[58] A. R. Edmonds. *Angular Momentum in Quantum Mechanics*. Princeton University Press, 1996.

[59] S. M. Wong. *Introductory nuclear physics*, chapter 3. Prentice Hall, 1990.

[60] P. Ring and P. Schuck. *The Nuclear Many-Body Problem*. Springer Verlag, NewYork, 1980.

[61] W. Greiner and J.A. Maruhn. *Nuclear Models*. Springer Verlag Berlin Heidelberg, 1996.

[62] C. Schwartz. Theory of hyperfine structure. *Phys. Rev.*, 97, 1955.

[63] J. Eichler and W.E. Meyerhof. *Relativistic Atomic Collisions*. Academic Press San Diego, 1995.

[64] A. N. Moskalev D. A. Varshalovich and V. K. Khersonskii. *Quantum Theory of Angular Momentum*. World Scientific Singapore, 1988.

[65] V. N. Kononov V. S. Shorin, V. M. Gribunin and I. I. Sidorova. Nucleosynthesis of elements: s-process. *Astrophys. J.*, 7(3), 1971.

[66] G. Schatz. Note on technetium in stars. *Astro. & Astrophys.*, 122:327–329, June 1983.

[67] Nuclear Structure and Decay Databases, 2016. URL http://www.nndc.bnl.gov.

[68] SPECTR-W3 Database on spectroscopic properties of atoms and ions, 2016. URL http://http://spectr-w3.snz.ru/ion.phtml.

[69] Peter J. Mohr, Barry N. Taylor, and David B. Newell. Codata recommended values of the fundamental physical constants: 2006. *Rev. Mod. Phys.*, 80:633–730, Jun 2008. doi: 10.1103/RevModPhys.80.633. URL http://link.aps.org/doi/10.1103/RevModPhys.80.633.

[70] I P. Grant F. A. Parpia, C. Froese Fischer. Grasp92: A package for large-scale relativistic atomic structure calculations. *Comp. Phys. Commun.*, 94, 1996.

[71] W. R. Johnson and G. Soff. The lamb shift in hydrogen-like atoms, $1 \leq z \leq 110$. *Atomic Data and Nuclear Data Tables*, 33(3), 1985.

Acknowledgments

First and foremost I would like to gratefully acknowledge the enthusiastic supervision of PD. Dr. Adriana Pálffy during this work. I appreciate all her contributions of time and ideas to make my Master experience meaningful and stimulating. I thank Prof. Dr. Christoph Keitel for allowing me to join his group at the Max Planck Institute and for providing me with work resources. I would like to thank Dr. Jonas Gunst and Dr. Yuanbin Wu for having been a constant source of help along the way. Zoila Eisenhauer is thanked for her assistance with technical problems and her positive energy – at all times. I am also grateful to the secretary Sibel Babacan, for assisting me in handling the paperwork. I offer my sincere gratitude to all my office mates — Dr. Stefano M. Cavaletto, Dr. Oleg Skoromnik, Dr. Sebastian Meuren, Alessandro Angioi, Sergey Bragin, and Halil Cakir — for contributing to a pleasant working atmosphere. Archana Sampath, Maitreyi Sangal and Yue-Yue Chen are especially thanked for their care and love.

I am deeply grateful to all my friends — Veronica Pizzella, Daniel Jiménez Tejero, Daniele Petillo, Qiongdan Zhang, Alexander Chatrchyan and Alberto Bailoni — from University of Heidelberg, for being the surrogate family in Heidelberg and for their continued moral support. I am also grateful to Julia Schäfer for her support.

Finally, I am forever indebted to my family for their understanding, endless patience and encouragement when it was most required.

Erklärung:

Ich versichere, dass ich diese Arbeit selbstständig verfasst habe und keine anderen als die angegebenen Quellen und Hilfsmittel benutzt habe.

Heidelberg, den (Datum) .....